Article

Cell Reports

Talin Autoinhibition Regulates Cell-ECM Adhesion Dynamics and Wound Healing *In Vivo*

Graphical Abstract

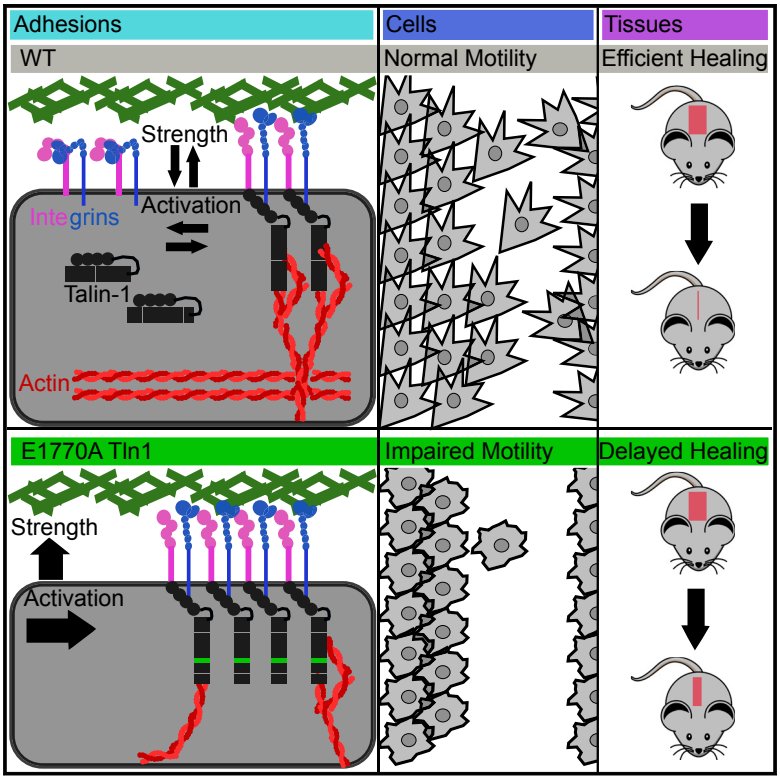

Authors

Amanda Haage, Katharine Goodwin, Austin Whitewood, ..., Sergey Plotnikov, Benjamin T. Goult, Guy Tanentzapf

Correspondence

tanentz@mail.ubc.ca

In Brief

Using a new transgenic mouse model that disrupts talin autoinhibition, Haage et al. characterize in quantitative detail the results of a wholesale increase in cell-ECM adhesion. Increasing adhesion delays wound healing due to a shift to more mature and stable adhesions, which inhibit dynamic cell movements.

Highlights

- Disrupting talin autoinhibition via E1770A mutation results in viable mice
- Disrupting talin autoinhibition delays wound healing *in vitro* and *in vivo*
- E1770A Talin increases focal adhesion maturity, stability, and strength
- E1770A Talin disrupts actin organization and traction force generation

Haage et al., 2018, Cell Reports *25*, 2401–2416
November 27, 2018 © 2018 The Authors.
https://doi.org/10.1016/j.celrep.2018.10.098

CellPress

Cell Reports
Article

OPEN ACCESS
CellPress

Talin Autoinhibition Regulates Cell-ECM Adhesion Dynamics and Wound Healing *In Vivo*

Amanda Haage,[1] Katharine Goodwin,[1] Austin Whitewood,[2] Darius Camp,[1] Aaron Bogutz,[3] Christopher T. Turner,[4] David J. Granville,[4] Louis Lefebvre,[3] Sergey Plotnikov,[5] Benjamin T. Goult,[2] and Guy Tanentzapf[1,6,*]

[1]Department of Cellular and Physiological Sciences, 2350 Health Sciences Mall, University of British Columbia, Vancouver, BC V6T 1Z3, Canada
[2]School of Biosciences, Giles Ln, University of Kent, Canterbury CT2 7NZ, UK
[3]Department of Medical Genetics, 2350 Health Sciences Mall, University of British Columbia, Vancouver, BC V6T 1Z3, Canada
[4]Department of Pathology and Laboratory Medicine, 2211 Wesbrook Mall, University of British Columbia, Vancouver, BC V6T 2B5, Canada
[5]Department of Cell and Systems Biology, 25 Harbord Street, University of Toronto, Toronto, ON M5S 3H7, Canada
[6]Lead Contact
*Correspondence: tanentz@mail.ubc.ca
https://doi.org/10.1016/j.celrep.2018.10.098

SUMMARY

Cells in multicellular organisms are arranged in complex three-dimensional patterns. This requires both transient and stable adhesions with the extracellular matrix (ECM). Integrin adhesion receptors bind ECM ligands outside the cell and then, by binding the protein talin inside the cell, assemble an adhesion complex connecting to the cytoskeleton. The activity of talin is controlled by several mechanisms, but these have not been well studied *in vivo*. By generating mice containing the activating point mutation E1770A in talin (*Tln1*), which disrupts autoinhibition, we show that talin autoinhibition controls cell-ECM adhesion, cell migration, and wound healing *in vivo*. In particular, blocking autoinhibition gives rise to more mature, stable focal adhesions that exhibit increased integrin activation. Mutant cells also show stronger attachment to ECM and decreased traction force. Overall, these results demonstrate that modulating talin function via autoinhibition is an important mechanism for regulating multiple aspects of integrin-mediated cell-ECM adhesion *in vivo*.

INTRODUCTION

Integrin-mediated adhesion to the extracellular matrix (ECM) contributes to multiple processes during animal development and tissue homeostasis. To allow integrins to perform diverse roles with a high degree of spatial and temporal specificity, integrin-mediated adhesion must be modulated rapidly and precisely (Iwamoto and Calderwood, 2015; Wolfenson et al., 2013). One of the best-characterized methods of regulation is integrin activation. During integrin activation, the integrin extracellular domain extends, which substantially increases its binding affinity for ECM ligands (Shattil et al., 1995). Integrin activation can be induced by interactions between the integrin cytoplasmic domain and various cytoplasmic factors (inside-out activation) or by interactions with insoluble extracellular ligands (outside-in activation) (Calderwood, 2004a; Ginsberg, 2014). In particular, the large cytoplasmic adaptor protein talin is known as a key player in inside-out activation, and the regulation of talin recruitment to the membrane modulates integrin activity (Calderwood, 2004b; Ginsberg, 2014).

Talin connects integrins to the rest of the adhesion complex by binding directly to the cytoplasmic tail of β-integrins and then connecting either directly, through its actin binding domains, or indirectly, via other adaptor proteins, to the cytoskeleton (Horwitz et al., 1986; Kanchanawong et al., 2010). Talin function is essential for cell-ECM adhesion, and it is required for assembly and maintenance of the integrin adhesion complex (Klapholz and Brown, 2017). Talin is a large cytoplasmic protein composed of a globular N-terminal head region, containing a FERM (protein 4.1, ezrin, radixin, and moesin) domain, and a flexible rod region. There are two known integrin binding sites (IBSs) in talin: IBS-1, located within the FERM domain, and IBS-2, at the C terminus (Critchley, 2009). The IBS-1 site in the FERM domain mediates inside-out activation by binding to the β-integrin cytoplasmic tail. This initiates a cascade of events resulting in conformational changes of the integrin extracellular domain that increase its affinity for ECM ligands (Tadokoro et al., 2003). Loss of talin in cells and in animal models largely phenocopies the loss of integrin function (Brown et al., 2002; Monkley et al., 2000; Priddle et al., 1998). Conversely, overexpression of the talin head domain is sufficient to induce inside-out integrin activation (Calderwood et al., 1999; Kim et al., 2003). Due to its central role in integrin-based adhesions, elucidating how talin function is regulated is important for a mechanistic understanding of how integrin-mediated cell-ECM adhesion is regulated.

Previously, talin function has been shown to be regulated by several mechanisms (Klapholz and Brown, 2017). Similar to other FERM domain-containing proteins, talin can form intramolecular autoinhibitory interactions between the FERM domain and other parts of the molecule (Goult et al., 2009). Previous biochemical experiments have shown that the talin head can interact with the talin rod. Cell culture experiments have further shown that mutations that block this interaction result in increased integrin activation (Goksoy et al., 2008; Kopp et al.,

This is an open access article under the CC BY-NC-ND license (http://creativecommons.org/licenses/by-nc-nd/4.0/).

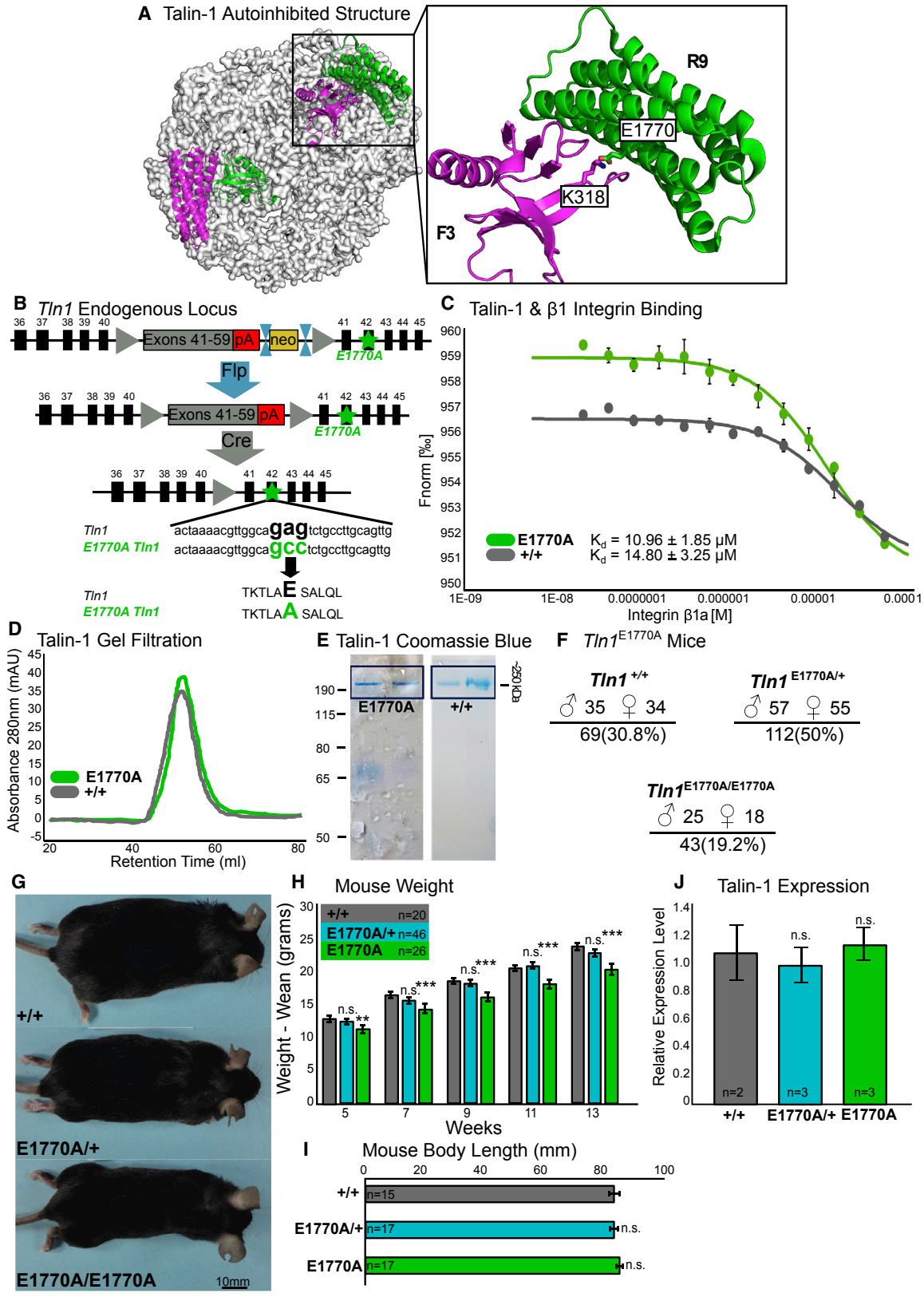

(legend on next page)

2010). Moreover, biochemical experiments have shown that the talin rod binds the same region in the talin head as β-integrin cytoplasmic tails. This suggests that these two interactions are mutually exclusive, which is consistent with autoinhibition (Goult et al., 2009). Cryoelectron microscopy (cryo-EM) analysis of full-length talin suggests that it forms a compact donut-shaped autoinhibited structure by dimerizing with another talin molecule (Goult et al., 2013). This allows many intra- and intermolecular interactions to form and stabilize the globular structure of talin in its autoinhibited, dimerized conformation (Zhang et al., 2016). Some evidence from cell culture experiments supports an important functional role for autoinhibition in regulating talin function. Cell fractionation experiments suggest that forcing talin into a non-autoinhibited or open conformation increases its localization to the membrane (Banno et al., 2012). In cultured human umbilical vein endothelial cell (HUVEC) cells transfected with *TLN1* small interfering RNA (siRNA) and an autoinhibition mutant rescue transgene, cell spreading was defective and there was an increased number of focal adhesions (FAs) (Kopp et al., 2010).

To date, the only characterization of the requirement for autoinhibition *in vivo* comes from experiments in *Drosophila*, in which endogenous Talin was replaced with mutant, autoinhibition-defective Talin (Ellis et al., 2013). This Talin autoinhibition mutant behaved in the manner expected from a gain-of-function allele, and morphogenetic defects were observed because of too much, rather than too little, adhesion (Ellis et al., 2013; Goodwin et al., 2016). These phenotypes were hypothesized to be due to enhanced recruitment and binding of Talin and integrins, as well as reduced Talin turnover at sites of adhesion. Consequently, morphogenetic processes that require cyclic adhesion assembly and disassembly were disrupted. In contrast, integrin-based adhesion at myotendinous junctions, a non-morphogenetic context involving adhesive structures that are more stable and persistent, is largely normal in Talin autoinhibition-defective flies (Ellis et al., 2013). Furthermore, detailed analysis of morphogenic events in Talin autoinhibition-defective flies showed that autoinhibition could regulate the large-scale biomechanical properties of cells and tissues. This defect was manifested in Talin autoinhibition-defective embryos as a failure to regulate cell migration and force transmission, leading to disrupted and delayed tissue development (Goodwin et al., 2016).

Here, we describe the phenotypic characterization of mice containing a mutation in talin (*Tln1*) that abrogates its ability to undergo autoinhibition ($Tln1^{E1770A}$). We confirm earlier cell culture observations that autoinhibition regulates the recruitment of Tln1 to sites of adhesion, including regulating FA size. Using comprehensive phenotypic analysis of mouse embryonic fibroblasts (MEFs) derived from $Tln1^{E1770A}$ embryos and a range of techniques including quantitative imaging, total internal reflection fluorescence (TIRF), and traction force microscopy, we were able to uncover diverse functional phenotypes. Phenotypes observed include effects at the level of single FAs, such as changes in composition and stability, as well as effects at the level of the entire cell, such as abnormal shape, behavior, and migration. Finally, we extend our analysis to tissue-level effects *in vivo* and show that Tln1 autoinhibition-defective mice exhibit impaired tissue repair following injury. Our results demonstrate the importance and versatility of Tln1 autoinhibition as a regulatory tool for controlling integrin-mediated cell-ECM adhesion *in vivo*.

RESULTS

Generation of a *Tln1* Autoinhibition-Defective Mouse Mutant

Previous structural and biochemical studies have mapped the autoinhibitory regions in Tln1 to the F3 lobe of the FERM domain (residues 306–400 in mouse Tln1) and R9 (rod domain 9), which forms an amphipathic helical bundle (residues 1,655–1,822). Point mutations have been identified in both the R9 and the FERM domains that block their interaction *in vitro* (Goult et al., 2009). However, the region of the FERM domain that is involved is known to have multiple roles, including binding to β-integrin cytoplasmic tails and PIP2. We therefore decided to mutate a residue from the R9 domain that *in vitro* abrogates binding with the FERM domain and thus blocks autoinhibition. The mutation selected changes a conserved glutamate residue in R9 (E1770 in mouse Tln1), which forms a buried salt bridge with the K318 residue in the FERM domain, to an alanine (E1770A) (Figures 1A and 1B). We confirmed that the overall stability and function of Tln1 was not compromised by the E1770A mutation using microscale thermophoresis and analytical gel filtration experiments. In particular, we observed that in 150 mM NaCl, both wild-type and E1770A mutant full-length Tln1 were able to bind to the cytoplasmic tail of β1-integrin

Figure 1. Talin Autoinhibition Is Not Essential for Viability in Mice

(A) Structure of the autoinhibited talin dimer. The gray envelope represents the autoinhibited dimer as visualized by electron microscopy (Goult et al., 2013). The two monomers are shown in green and purple. Inset: the structure of the F3:R9 complex (PDB: 4F7G) (Song et al., 2012) with the key buried salt bridge between R9 E1770 and F3 K318 highlighted.

(B) Schematic of the mutagenesis of the E1770A site in *Tln1*.

(C) Microscale thermophoresis assay demonstrating binding of RED-Tris-NTA-labeled full-length Tln1 wild-type (gray) and E1770A (green) to the β1a-integrin peptide.

(D) Gel filtration (Superdex 200) elution profiles of purified recombinant wild-type (gray) and E1770A Tln1 (green).

(E) Coomassie-stained SDS-PAGE gel of purified recombinant wild-type and E1770A Tln1.

(F) Genotyping results of 40 $Tln1^{E1770A/+}$ intercrosses (224 mice total). The observed segregation ratio is statistically significant with a chi-square test, $p < 0.05$.

(G) Male mice at 21 weeks of age.

(H) Male mouse weight over time minus weight at weaning.

(I) Mouse body length measured from nose tip to base of tail of male mice 18–22 weeks of age.

(J) Relative Tln1 expression levels determined via qRT-PCR from MEFs.

All error bars denote SEM, with ***$p \leq 0.0001$, **$p \leq 0.001$, and *$p \leq 0.01$.

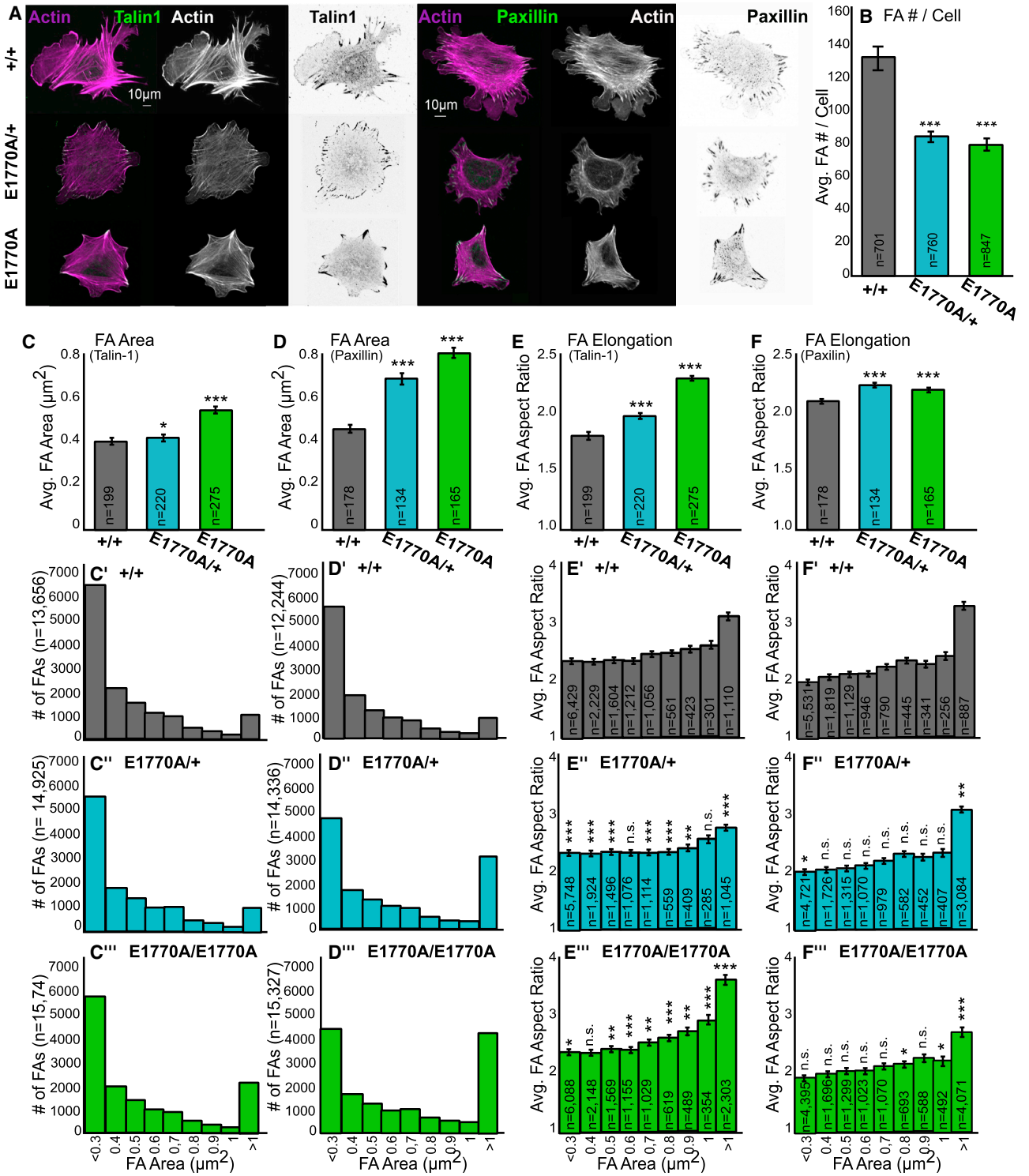

Figure 2. Talin Autoinhibition Regulates FA Maturation

(A) Representative images of MEFs derived from *Tln1*^{E1770A} mutant embryos plated on fibronectin and stained with a TLN1-specific antibody or a Paxillin-specific antibody (green is black in inverted images; actin is magenta or white).

(B) *Tln1*^{E1770A} mutant MEFs have a significantly reduced average number of FAs per cell.

(C) The average FA area per cell marked by Tln1 staining. n values in (C) represent cells. Data are binned in groups ranging from less than 0.3 μm^2 to more than 1 μm^2 for each genotype, with (C′) *Tln1*$^{+/+}$, (C″) *Tln1*$^{E1770A/+}$, and (C‴) *Tln1*$^{E1770A/E1770A}$. n values for data in (C′)–(C‴) represent FAs.

(legend continued on next page)

with similar affinity (Figure 1C) and that both proteins have the same gel filtration elution profile (Figures 1D and 1E). We then generated mice containing the *Tln1*^{E1770A} mutation (see STAR Methods). These mice were viable and fertile (Figure 1F) and did not exhibit gross morphological defects (Figure 1G). However, the number of live *Tln1*$^{E1770A/E1770A}$ homozygotes recovered at weaning from intercrosses between heterozygous mice was slightly below the expected Mendelian ratio: 19.2% instead of 25% (n = 224, p = 0.0489) (Figure 1F). This could suggest a slight survival disadvantage in the homozygous mutants. In addition, *Tln1*$^{E1770A/E1770A}$ mice exhibited a small but statistically significant reduction in weight gain compared to *Tln1*$^{+/+}$ controls or *Tln1*$^{E1770A/+}$ mice (Figures 1G and 1H). Despite this, their overall body length was normal (Figure 1I). To ensure that the phenotypes observed were specifically due to the E1770A mutation, we confirmed that Tln1 was expressed at normal levels in primary MEF cultures derived from *Tln1*$^{+/+}$, *Tln1*$^{E1770A/+}$, and *Tln1*$^{E1770A/E1770A}$ mutant embryos (Figure 1J).

Talin Autoinhibition Regulates FA Maturation in MEFs

To investigate the effect of the E1770A mutation on FAs, we isolated primary cultures of MEFs from *Tln1*$^{+/+}$, *Tln1*$^{E1770A/+}$, and *Tln1*$^{E1770A/E1770A}$ mutant embryos at embryonic day 13.5 (E13.5). We comprehensively analyzed the FA number, composition, and shape in these fibroblasts using multiple markers and high-resolution, quantitative, automated image analysis (Figure 2). In MEFs from all three genotypes analyzed, characteristic FAs and stress fibers were present that contained typical markers (Figure 2A). The average number of FAs per cell was lower by about a third in *Tln1*$^{E1770A/+}$ and *Tln1*$^{E1770A/E1770A}$ mutant MEFs (Figure 2B). Though there were fewer total FAs, the FAs observed in *Tln1*$^{E1770A/+}$ and *Tln1*$^{E1770A/E1770A}$ mutant MEFs were on average larger in area (Figures 2C and 2D), and plotting histograms showing the distribution of areas across the genotypes revealed a large increase in the number of FAs more than 1 μm^2 in size (Figures 2C and 2D). The increased size of FAs in the presence of *Tln1*^{E1770A} is consistent with the presence of more mature adhesions. A characteristic of maturing adhesions is that as they increase in area, they also elongate (Geiger and Yamada, 2011; Wolfenson et al., 2009). We determined that the average aspect ratio of FAs in MEFs from *Tln1*$^{E1770A/+}$ and *Tln1*$^{E1770A/E1770A}$ embryos was also larger compared to *Tln1*$^{+/+}$ MEFs. This increase in aspect ratio was consistent across the spectrum of the FA area, plotted in relation to the FA area (Figures 2E and 2F). These measurements revealed that the *Tln1*^{E1770A} mutation increased the number of larger, more elongated adhesions, consistent with an overall increase in FA maturation.

Talin Autoinhibition Regulates Integrin Activation and Integrin Signaling

Increased FA maturation is associated with higher integrin activation (Lee et al., 2013), which might be one predicted outcome of lower Tln1 autoinhibition. To test whether the *Tln1*^{E1770A} mutation promoted integrin activation, we used the active β1-integrin-specific antibody 9EG7 (Bazzoni et al., 1995). MEFs from *Tln1*$^{+/+}$, *Tln1*$^{E1770A/+}$, and *Tln1*$^{E1770A/E1770A}$ embryos were co-stained using a general β1-integrin antibody and 9EG7. The ratio of the staining intensity of these two antibodies within FAs was used to measure activation. These data showed a significant increase in integrin activation in *Tln1*^{E1770A} mutant MEFs (Figures 3A and 3B). In addition, *Tln1*^{E1770A} mutants had increased co-localization of both Tln1 and paxillin with either general β1-integrin or active β1-integrin, though this effect was more striking with activated β1-integrin (Figure 3E; Figures S1 and S2). All of these data are consistent with higher integrin activation in *Tln1*^{E1770A} mutants. Integrin activation is closely linked with modulation of integrin signaling (Clark and Brugge, 1995). The phosphorylation of focal adhesion kinase (FAK) at Y397 is a useful marker for activation of integrin signaling. FAK phosphorylation was similarly assessed by co-staining MEFs from *Tln1*$^{+/+}$, *Tln1*$^{E1770A/+}$, and *Tln1*$^{E1770A/E1770A}$ embryos with antibodies that detect either all FAK protein or phosphorylated FAK(Y397) specifically. The ratio of intensity between these two antibodies was measured within FAs and showed increased phosphorylation of FAK at Y397 in *Tln1*^{E1770A} mutant MEFs (Figures 3C and 3D). Altogether, these results suggest an increase in both integrin activation and signaling in the presence of the *Tln1*^{E1770A} mutation.

Talin Autoinhibition Regulates FAs Stability

Because an increase in either FA maturation or integrin activation would be consistent with increased FA stability, we analyzed FA dynamics in MEFs from *Tln1*$^{+/+}$, *Tln1*$^{E1770A/+}$, and *Tln1*$^{E1770A/E1770A}$ embryos. FA dynamics were analyzed in two ways. First, FRAP (fluorescence recovery after photobleaching) was used to determine the mobile fraction of three FA markers: paxillin-GFP (Figures 4A and 4B; Figures S3A–S3C), Tln1-GFP (Figures 4C and 4D), and Tln1-GFP containing the E1770A point mutation (Figures 4E and 4F). This analysis showed that the mobile fraction of paxillin-GFP and Tln1-GFP in FAs in *Tln1*$^{E1770A/E1770A}$ MEFs was ~28% and ~40% lower, respectively, compared to controls (Figures 4A–4D). The mobile fraction of paxillin-GFP in FAs in *Tln1*$^{E1770A/+}$ MEFs was not significantly different (Figures S4A and S4B). Introducing the E1770A point mutation into Tln1-GFP resulted in a 66% reduction in the mobile fraction compared to the wild-type construct in *Tln1*$^{+/+}$ MEFs (Figures 4E and 4F). Furthermore, for the Tln1-GFP containing

(D) The average FA area per cell marked by paxillin staining. n values in (D) represent cells. Data are binned in groups ranging from less than 0.3 μm^2 to more than 1 μm^2 for each genotype, with (D′) *Tln1*$^{+/+}$, (D″) *Tln1*$^{E1770A/+}$, and (D‴) *Tln1*$^{E1770A/E1770A}$. n values in (D′)–(D‴) represent FAs.

(E) The average FA aspect ratio (length/width) per cell marked by Tln1 staining. n values in (E) represent cells. Data are binned in groups ranging from a less than 0.3 μm^2 area to a more than 1 μm^2 area for each genotype, showing the average aspect ratio for each group, with (E′) *Tln1*$^{+/+}$, (E″) *Tln1*$^{E1770A/+}$, and (E‴) *Tln1*$^{E1770A/E1770A}$. n values for data in (E′)–(E‴) represent FAs.

(F) The average FA aspect ratio (length/width) per cell marked by paxillin staining. n values in (F) represent cells. Data are binned in groups ranging from a less than 0.3 μm^2 area to a more than 1 μm^2 area for each genotype, showing the average aspect ratio for each group, with (F′) *Tln1*$^{+/+}$, (F″) *Tln1*$^{E1770A/+}$, and (F‴) *Tln1*$^{E1770A/E1770A}$. n values for data in (F′)–(F‴) represent FAs.

All error bars denote SEM, with ***p ≤ 0.0001, **p ≤ 0.001, and *p ≤ 0.01.

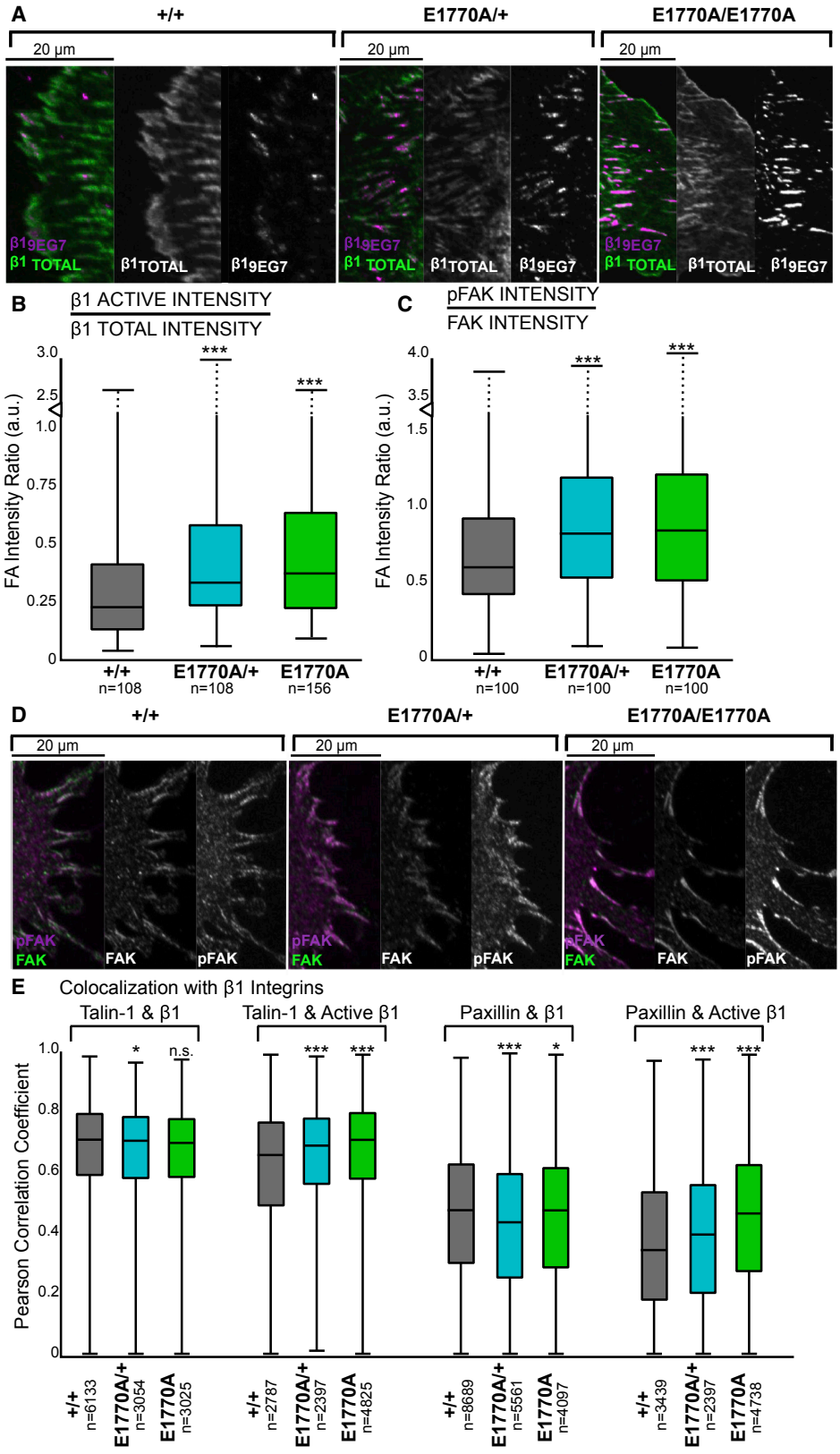

(legend on next page)

the E1770A point mutation, similar mobile fractions were observed in either *Tln1*$^{+/+}$ or *Tln1*$^{E1770A/E1770A}$ MEFs, consistent with the autoinhibition-defective Talin already being present in *Tln1*$^{E1770A/E1770A}$ MEFs (Figures 4E and 4F). Second, TIRF microscopy was employed, using paxillin-GFP as a marker to analyze FA dynamics. To study their dynamics, FAs in *Tln1*$^{+/+}$, *Tln1*$^{E1770A/+}$, and *Tln1*$^{E1770A/E1770A}$ MEFs were imaged over the course of 1 hr (Figure 4G). Analysis of the TIRF data revealed a small but significant increase in the average longevity of FAs (Figure 4H). To relate FA stability and maturation, we looked at the percentage of FAs per cell that were either small and short lived (Figure 4I, nascent FAs) or large and stable (Figure 4J, mature FAs) across the genotypes. Both *Tln1*$^{E1770A/+}$ and *Tln1*$^{E1770A/E1770A}$ MEFs had a significant decrease in the percentage of nascent FAs per cell and a significant increase in the percentage of mature FAs per cell (Figures 4I and 4J). In addition, we looked at the lifetime of tracked FAs using a previously established modeling method in which the duration and slopes of the assembly, stability, and disassembly phases of FAs are shown to scale (Berginski et al., 2011). Both *Tln1*$^{E1770A/+}$ and *Tln1*$^{E1770A/E1770A}$ MEFs showed greater assembly and a longer duration of the stability phase compared to control MEFs (Figure 4K, homozygous example only). Altogether, our data show that FAs in MEFs derived from *Tln1*^{E1770A} mutants are longer lasting and more stable than FAs in controls.

The *Tln1*^{E1770A} Phenotype Is Independent of Tln2

It is known that in some instances, loss of Tln1 is compensated by increased expression of the talin 2 (Tln2) gene (Zhang et al., 2008). We wanted to determine whether, similarly, the *Tln1*^{E1770A} phenotype was modified by changes in expression of Tln2. Relative levels of Tln2 protein expression were analyzed in MEFs from *Tln1*$^{+/+}$, *Tln1*$^{E1770A/+}$, and *Tln1*$^{E1770A/E1770A}$ embryos. This analysis showed that overall levels of Tln2 were not significantly changed (Figure S3A). We then performed a siRNA knockdown of Tln2 in *Tln1*$^{+/+}$ and *Tln1*$^{E1770A/E1770A}$ MEFs (Figures S3B–S3J). Western blot analysis confirmed that the siRNA produced a robust knockdown of the Tln2 protein (Figure S3B). Loss of Tln2 did not have the dramatic effect on FA formation seen in MEFs that lack Tln1 (Zhang et al., 2008), although FAs were slightly smaller (Figures S3C and S3D). When Tln2 knockdown was performed in the background of the *Tln1*^{E1770A} mutation, there was no substantial or consistent enhancement or suppression of the E1770A phenotype beyond the reduction of FA size seen in *Tln1*$^{+/+}$ MEFs (Figures S3E and S3F). Knockdown of Tln2 did not alter the relative difference in FA dynamics between *Tln1*$^{+/+}$ and *Tln1*$^{E1770A/E1770A}$ mutants (Figures S3G–S3J). Altogether, these results argue that the *Tln1*^{E1770A} phenotype is independent of Tln2.

Talin Autoinhibition Regulates Adhesion Strength and Cell Spreading in MEFs

The changes in FAs observed in *Tln1*^{E1770A} mutants would be expected to affect aspects of cell-ECM adhesion and cell morphology. To assess the strength of cell-ECM adhesions, we adapted an assay that uses a cell-spinning device (García et al., 1997) to determine the relative attachment strength of cells to an underlying ECM. In this assay, cells are incubated on fibronectin-coated coverslips and allowed to attach. Following attachment, they are spun, exposing them to centrifugal force and detaching more loosely affixed cells. Relative adhesion strength is then calculated by determining the ratio of cells attached after spinning compared to a same-day non-spun control. This technique revealed that *Tln1*^{E1770A} mutant MEFs showed stronger attachment to the ECM relative to *Tln1*$^{+/+}$ MEFs (Figures 4L and 4M). Moreover, MEFs from either *Tln1*$^{E1770A/+}$ or *Tln1*$^{E1770A/E1770A}$ mutant embryos exhibited a spreading defect. When plated on fibronectin, they exhibited reduced growth in cell area over 90 min compared to controls (Figures 5A and 5B). This spreading phenotype was not due to a defect in the initial attachment of cells, because both mutant and control cells adhered to the ECM-coated coverslips equally well (Figure 5C). The morphology of *Tln1*$^{E1770A/+}$ or *Tln1*$^{E1770A/E1770A}$ MEFs was also different from that of *Tln1*$^{+/+}$ MEFs (Figure 5A). Calculating the cell aspect ratio and circularity of MEFs from *Tln1*$^{E1770A/E1770A}$ embryos showed that they were rounder than *Tln1*$^{+/+}$ controls (Figures 5D and 5E). In line with this, there was a reduction in the number of actin-based cell protrusions in *Tln1*^{E1770A} mutant MEFs, and these protrusions were shorter and thicker compared to *Tln1*$^{+/+}$ (Figures 5F and 5H). This defect did not improve with time (Figure 5G). The cell-spreading defects that we observed could result from defects in the formation of nascent adhesions. We analyzed nascent adhesion formation by using Paxillin-GFP and TIRF microscopy to track adhesion formation and assembly rate during cell spreading (Figures S4D–S4H). We found that *Tln1*$^{E1770A/E1770A}$ mutant MEFs exhibit longer-lasting FAs and that there is a decrease in the rate of formation of nascent adhesions and a corresponding increase in the rate of formation of mature adhesions (Figures S4E–S4G). Altogether, these results show that *Tln1*^{E1770A} mutant MEFs not only show increased adhesion strength to their ECM ligands, but also exhibit persistent defects in cell spreading and actin-based cell protrusions. These defects, which possibly occur due to reduced ability to form

Figure 3. Talin Autoinhibition Regulates Integrin Activation and Signaling

(A) Representative images of the leading edge of MEFs plated on fibronectin and stained with the active β1-integrin-specific monoclonal antibody 9EG7 (magenta) and a polyclonal β1-integrin antibody (green).

(B) Ratio of FA intensities of the stainings represented in (A) of active β1-integrin to total β1-integrin. n values represent numbers of cells.

(C) Ratio of FA intensities of stainings represented in (D) of phosphorylated FAK (phosphoFAK) to total FAK. n values represent numbers of cells.

(D) Representative confocal images of the leading edge of MEFs plated on fibronectin and stained with a phosphoFAK-specific monoclonal antibody (Y397, magenta) and a polyclonal FAK antibody (green).

(E) Pearson correlation coefficients of FA markers. See also Figures S1 and S2. n values represent numbers of FAs, and only FAs with positive correlation were included.

All error bars denote SEM, with ***$p \leq 0.0001$, **$p \leq 0.001$, and *$p \leq 0.01$.

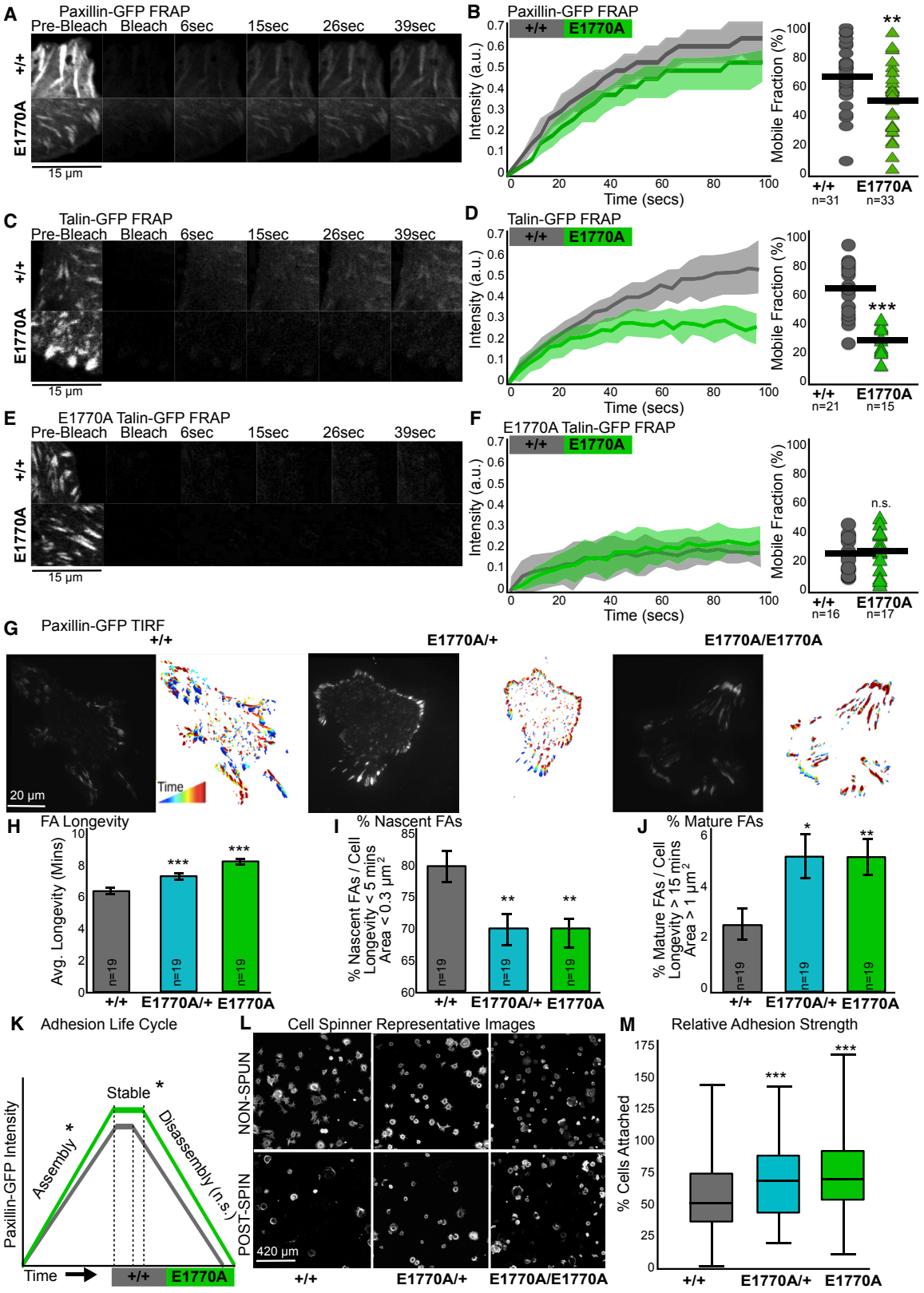

(legend on next page)

nascent FAs, result in a rounder appearance of the cells compared to wild-type controls.

Talin Autoinhibition Regulates Wound Healing Both *In Vitro* and *In Vivo*

Although several phenotypes were observed in *Tln1*^{E1770A} mutant MEFs, including abnormal integrin activation and signaling, increased adhesion, reduced cell protrusions, and defective cell spreading, it was unclear whether these would result in a functional defect. One possible effect of such phenotypes is a defect in cell migration. Therefore, cell migration was assessed in the background of the *Tln1*^{E1770A} mutation using a scratch assay, a well-established *in vitro* assay for cell migration (Liang et al., 2007). This analysis showed that both *Tln1*$^{E1770A/+}$ and *Tln1*$^{E1770A/E1770A}$ MEFs exhibited delayed wound closure compared to *Tln1*$^{+/+}$ controls (Figures 6A and 6B). Because fibroblasts also migrate to close wounds *in vivo*, the effects of the *Tln1*^{E1770A} mutation were analyzed in a biopsy punch wound healing assay in mice (Ganguli-Indra, 2014) (Figures 6C and 6D). Statistically significant delays in wound closure were observed in both *Tln1*$^{E1770A/+}$ and *Tln1*$^{E1770A/E1770A}$ mutant mice, though the wounds eventually closed. Overall, these data suggest that regulation of Tln1 function by autoinhibition is important for cell migration in MEFs and, more generally, for wound healing in mice.

Talin Autoinhibition Regulates Actin Organization and Traction Force in MEFs

We hypothesized that the wound healing phenotypes seen in *Tln1*^{E1770A} mutants were in part due to abnormal traction force, because the ability of fibroblasts to generate traction forces is thought to be essential for multiple stages of wound closure (Li and Wang, 2011; Tomasek et al., 2002) To investigate this, we measured the total traction force generated by MEFs derived from *Tln1*$^{+/+}$, *Tln1*$^{E1770A/+}$, and *Tln1*$^{E1770A/E1770A}$ embryos using traction force microscopy (Figure 7A). Surprisingly, we found that both total traction force (Figure 7B) and traction force per cell area (Figure 7C) were markedly reduced in *Tln1*^{E1770A} mutant MEFs compared to *Tln1*$^{+/+}$. This result was unexpected, because larger and/or more stable FAs, such as those seen in *Tln1*^{E1770A} mutant MEFs, are typically associated with higher traction forces (Ballestrem et al., 2001; Munevar et al., 2001). However, because lower traction forces can be associated with altered actin dynamics (Gardel et al., 2008; Thievessen et al., 2013; Tojkander et al., 2015), we used live imaging and various quantitative approaches to analyze the actin cytoskeleton. First, to quantitatively describe actin fibers within these cells, we adapted a previously described method (Cetera et al., 2014) to provide a measurement of the overall level of actin alignment. In *Tln1*^{E1770A} mutant MEFs, there is an overall decrease in the alignment of actin (Figure 7D). Specifically, the percentage of the cell that contains aligned bundles, termed cell fibrousness, is smaller in both *Tln1*$^{E1770A/+}$ and *Tln1*$^{E1770A/E1770A}$ mutant MEFs (Figure 7E). Moreover, the defects in actin alignment persist over time as cells spread (Figure 7F). Second, to directly study actin dynamics, the live cell actin marker F-tractin-GFP (Belin et al., 2014) was used to track actin behavior in MEFs. Using kymograph analysis over time within active cell protrusions (Figure 7G), the flow rate of actin in *Tln1*^{E1770A} mutant MEF protrusions was shown to be higher than controls (Figure 7H). When we controlled for cell shape by limiting our analysis to cells with a similar aspect ratio, actin flow rate was still higher in *Tln1*^{E1770A} mutant MEFs compared to *Tln1*$^{+/+}$ (Figure 7I). In addition, to directly study actin dynamics, a previously described modified FRAP technique (Tojkander et al., 2015) was used in cells in which the FAs were labeled with a live mCherry-paxillin marker (Figures 7K–7M). Here, areas of dorsal stress fibers directly adjacent to FAs were bleached, and kymograph analysis of the recovery was used to determine actin polymerization rate. *Tln1*$^{E1770A/E1770A}$ mutant MEFs exhibited a small but significant shift to a slower actin polymerization rate in dorsal stress fibers (Figure 7M). These results indicate that, consistent with lower traction force, *Tln1*$^{E1770A/E1770A}$ MEFs have a more dynamic actin cytoskeleton. Global FA organization has previously been shown to be important for the formation of an organized and efficient contractile actin network. This was measured using a previously established method (Wu et al., 2012) that assigns a value to the degree of distribution of FA angles in a cell, termed the FA

Figure 4. Talin Autoinhibition Regulates FA Stability and Adhesion Strength in MEFs

(A) Representative images of the leading edge of MEFs plated on fibronectin and transfected with paxillin-GFP (white). Region of interests (ROIs) were bleached, and recovery was imaged over time.

(B) Average recovery intensity over time (solid) with 95% confidence intervals (shaded) and mobile fractions, with a black line representing the mean. See also Figures S4A–S4C.

(C) Representative images of the leading edge of MEFs plated on fibronectin and transfected with Talin-1-GFP (white). ROIs were bleached, and recovery was imaged over time.

(D) Average recovery intensity over time (solid) with 95% confidence intervals (shaded) and mobile fractions, with a black line representing the mean.

(E) Representative images of the leading edge of MEFs plated on fibronectin and transfected with E1770A Talin-1-GFP (white). ROIs were bleached, and recovery was imaged over time.

(F and G) Average percentage of total FAs per cell meeting each criterion is presented per genotype. (F) Average recovery intensity over time (solid) with 95% confidence intervals (shaded) and mobile fractions, with a black line representing the mean. (G) Representative TIRF images stacked over 60 min of MEFs plated on fibronectin and transfected with paxillin-GFP (white). Maximum intensity images were colored based on time point and overlaid.

(H) Average minutes persisted throughout TIRF imaging.

(I) Nascent FAs, defined as lasting <5 min and area < 0.3 μm^2, were counted per cell.

(J) Mature FAs, defined as lasting >15 min and area > 1 μm^2, were counted per cell.

(K) Summary of FA life cycle, with the duration of each phase (length) and rates (slope) presented to scale.

(L) Representative images of MEFs plated on fibronectin and spun at 4,000 rpm compared to non-spun controls.

(M) Cell counts for cell-spinning assay per genotype. All n values represent numbers of cells.

All error bars denote SEM, with ***$p \leq 0.0001$, **$p \leq 0.001$, and *$p \leq 0.01$.

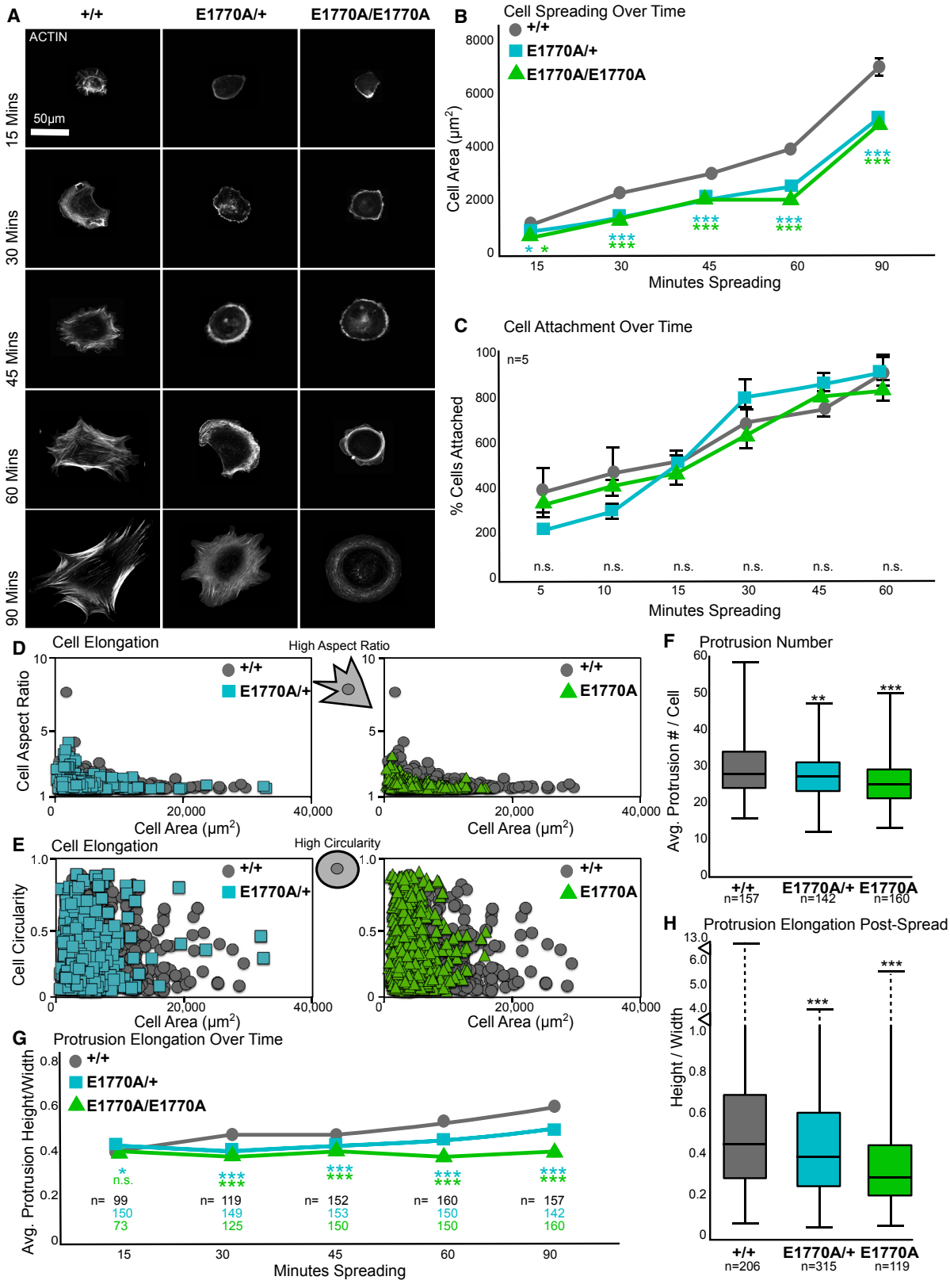

(legend on next page)

alignment index (FAAI). Surprisingly, despite the loss of actin fiber alignment and the increase in flow rate (Figures 7A–7I, 7L, and 7M), the average FAAI increased in *Tln1*^{E1770A} mutant MEFs (Figure 7J). Altogether, our data show that *Tln1*^{E1770A} mutant MEFs exhibit a reduction in traction force consistent with a less organized and more dynamic actin cytoskeleton. However, these changes in actin architecture appear to be decoupled from the organization of FAs. This loss of interdependence between actin and FA organization could contribute to the reduction in traction force generation.

DISCUSSION

Here we report the characterization of a mouse mutant that disrupts talin autoinhibition. Although these mice are viable, analysis of MEFs revealed several defects consistent with increased FA maturation and stability, as well as increased activation of integrins. Furthermore, MEFs from talin autoinhibition-defective mice exhibit stronger adhesion to the substrate, defective cell spreading, abnormal morphology, and cell migration defects. These defects have functional consequences in adult mice as revealed by *in vivo* wound healing assays. Finally, MEFs from talin autoinhibition-defective mice produce lower traction force but show increased actin dynamics. Our results reveal the importance of the regulatory mechanisms that fine-tune integrin-mediated cell-ECM adhesion *in vivo*. Moreover, they establish *Tln1*^{E1770A} mice as a useful tool to explore the range of phenotypes caused by increased talin activity in diverse cellular contexts.

Tln1$^{E1770A/E1770A}$ mice are viable and do not exhibit any of the dramatic morphological defects that are known to occur when integrin-mediated cell-ECM adhesion is disrupted. However, MEFs derived from these mice displayed a range of defects. How can we reconcile these somewhat contradictory observations? Many cellular phenotypes identified in *Tln1*^{E1770A} mutant MEFs were subtle and only became apparent after detailed quantitative analysis. This may be because many functionally overlapping regulatory mechanisms act on integrin-mediated adhesion (Iwamoto and Calderwood, 2015). However, it is also likely that regulatory mechanisms such as talin autoinhibition exhibit a tissue- and process-specific requirement. Thus, while we observe noticeable defects on the cellular or subcellular FA level in *Tln1*^{E1770A} MEFs, these defects only become apparent on the gross scale in specific contexts, such as wound healing. We believe that as we explore other cellular and tissue-specific contexts in greater detail, we will uncover additional phenotypes associated with defective talin autoinhibition.

Gain-of-function approaches provide the possibility of identifying novel functional requirements for genes in tissues and cells that are too disrupted in a simple loss-of-function mutant. Our goal in making the *Tln1*^{E1770A} mice was to produce a mutant that modulates talin function in a positive direction, because no such tool was available previously. Several lines of evidence presented here support the conclusion that disrupting talin autoinhibition gives rise to a gain-of-function allele. One risk of a gain-of-function approach is the possibility that it will affect processes that are not regulated by the wild-type form of the protein. However, the phenotypes observed in *Tln1*^{E1770A} mutants are in line with what would be expected from hyperactivated talin: increased integrin activity and signaling, stronger adhesion, and more recruitment of adhesion complex components. Nonetheless, in a few contexts, for example, in cell spreading, the *Tln1*^{E1770A} phenotype resembles a loss of function. These results are reminiscent of previous observations in similarly mutated flies. In the case of the Talin autoinhibition-defective mutant fly, it was proposed that phenotypes that resemble those seen in loss-of-function mutants occur when cellular function requires precise regulation of the level of adhesion and too much or too little adhesion disrupts the process to similar extents (Ellis et al., 2013; Goodwin et al., 2016). The *Tln1*^{E1770A} mutant behaves like a dominant mutation, because we observed phenotypes in both heterozygous and homozygous contexts. Here, the dosage of the *Tln1*^{E1770A} allele corresponded to the strength of the effect, with homozygous giving rise to stronger phenotypes than heterozygous. Overall, *Tln1*^{E1770A} mutant mice represent a versatile tool for manipulating the level of integrin-mediated cell-ECM adhesion *in vivo*. Given the ubiquity of talin and its central role in many types of integrin-based adhesions, we expect the *Tln1*^{E1770A} to be useful in future studies.

Using our gain-of-function approach, we identify a requirement for modulation of integrin-based adhesion during wound healing. Wound closure requires coordination of tissue-scale deformations, matrix assembly, and cell migration (Sakar et al., 2016). During wound healing, fibroblasts migrate to sites of injury and are one of the cell types that differentiate into myofibroblasts. These cells then assist wound closure by synthesizing ECM and by generating contractile forces that bring together the edges of the wound (Li and Wang, 2011). The wound healing phenotype we observe in *Tln1*^{E1770A} mutants could represent a defect in fibroblast recruitment and/or myofibroblast

Figure 5. Talin Autoinhibition Regulates Cell Spreading in MEFs

(A) Representative images of MEFs plated on fibronectin with actin stained by phalloidin (white).

(B) Average cell area was calculated at 15 min intervals over the course of 90 min. n values represent numbers of cells and are the same as in (G). Error bars are small enough that they are contained within the data marker.

(C) The average number of cells attached, calculated at 15 min intervals over the course of 60 min and shown as the percentage of attached cells at the final time point (90 min).

(D) Cell elongation, defined as the aspect ratio of the cell, plotted against cell area.

(E) Cell circularity, defined as 4π area/perimeter^2, is plotted against cell area. n values are same as in (G) at 90 min.

(F) Average number of actin-based protrusions per cell at 90 min. Protrusions were determined from phalloidin stains, counting instances in which there is a minimal distance between the cell contour and the convex hull (see STAR Methods).

(G) Average protrusion shape, measured as protrusion height (length from cell center) divided by width, calculated at 15 min intervals over the course of 90 min.

(H) Average protrusion elongation per cell at 90 min. n values represent numbers of cells and are the same as in (F). See also Figures S4D–S4H.

All error bars denote the SEM, with ***$p \leq 0.0001$, **$p \leq 0.001$, and *$p \leq 0.01$.

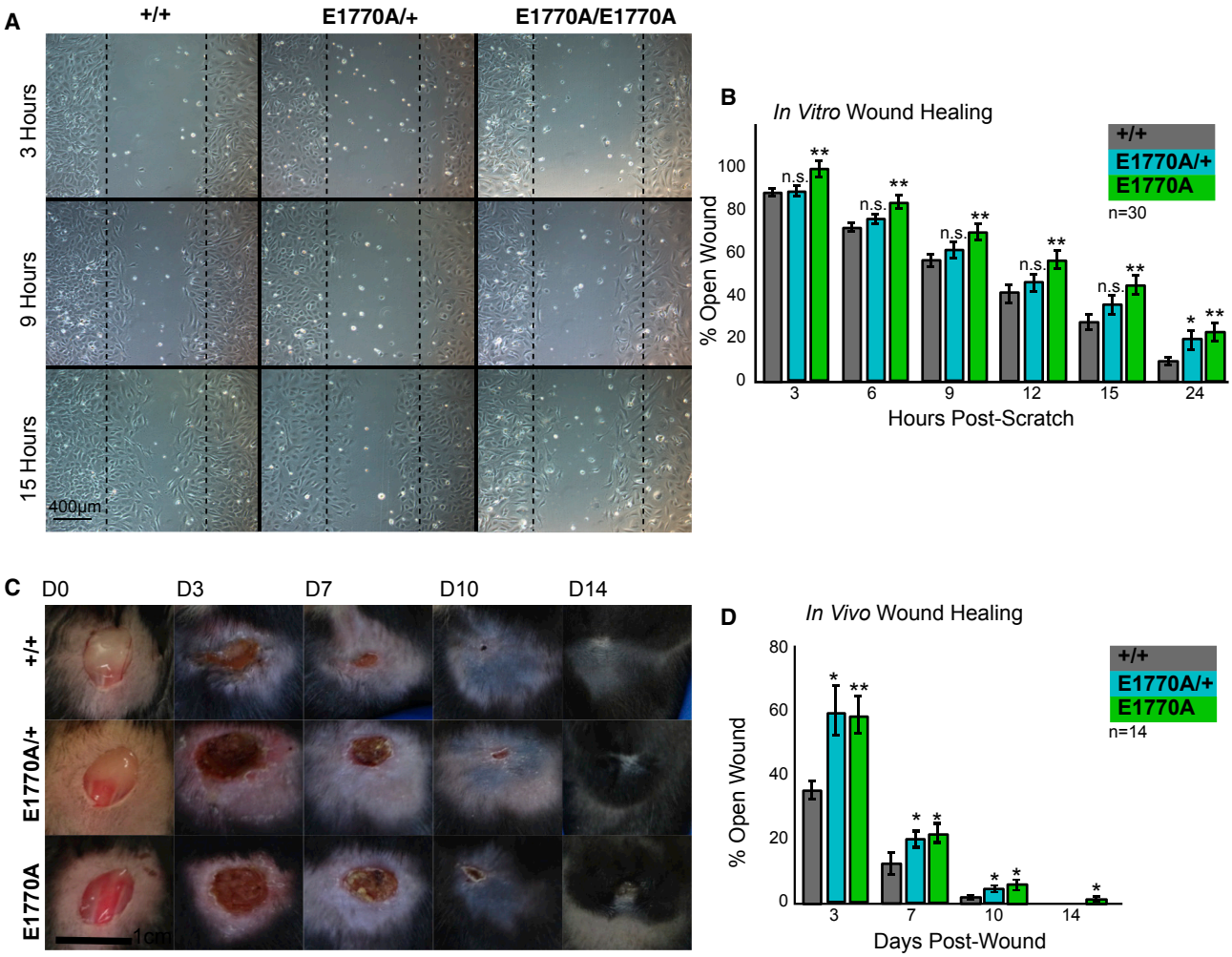

Figure 6. Talin Autoinhibition Regulates Wound Healing Both *In Vitro* and *In Vivo*

(A) Representative images of MEFs plated on fibronectin 3, 9, and 15 hr after a scratch is introduced in the monolayer with a pipette tip. The dotted line represents the wound edge at time 0.

(B) Average area of open wound per genotype, shown as the percentage of wound area at time 0, calculated at 3 hr intervals over the course of 24 hr.

(C) Representative images of biopsy punch wounds induced on the dorsal side of mice over 14 days.

(D) Average area of open wound per genotype for biopsy punches, shown as the percentage of area at initial wounding.

All error bars denote SEM, with ***p $\leq$ 0.0001, **p $\leq$ 0.001, and *p $\leq$ 0.01.

contractility. Our data show that the *Tln1*^{E1770A} mutation disrupts actin dynamics and gives rise to lower traction force in fibroblasts. Additional insight into how increased adhesion could give rise to a wound healing delay comes from our previous work on dorsal closure during fly embryogenesis (Ellis et al., 2013; Goodwin et al., 2016). Dorsal closure involves the sealing of a gap between two lateral sheets of epidermis and is an important model for animal morphogenesis and wound healing. There are strong parallels between wound healing in vertebrates and mechanisms of dorsal closure (Martin and Parkhurst, 2004). Integrin and Talin are essential for this process, and their absence results in defective closure, which leaves a dorsal hole in the embryo and causes embryonic lethality (Brown et al., 2002; Narasimha and Brown, 2004). Our work in flies has shown that Talin autoinhibition-defective mutants also have defects in dorsal closure and that these are due to the disruption of the biomechanical properties of the tissue (Ellis et al., 2013; Goodwin et al., 2016). In particular, we find that Talin autoinhibition mutants exhibit features consistent with increased cell-ECM adhesion, as well as problems in the regulation of the transmission of mechanical forces generated by actomyosin-based contractility. It is striking that in the context of wound closure in mice, we again encounter similar defects involving changes in adhesion, cell morphology, and mechanical force. This suggests conservation in the requirement for mechanisms that regulate cell-ECM adhesion during morphogenetic processes that mediate wound closure.

Our work shows that autoinhibition regulates multiple aspects of FA structure and function, because *Tln1*^{E1770A} mutants exhibit changes in the shape, size, composition, actin dynamics, and

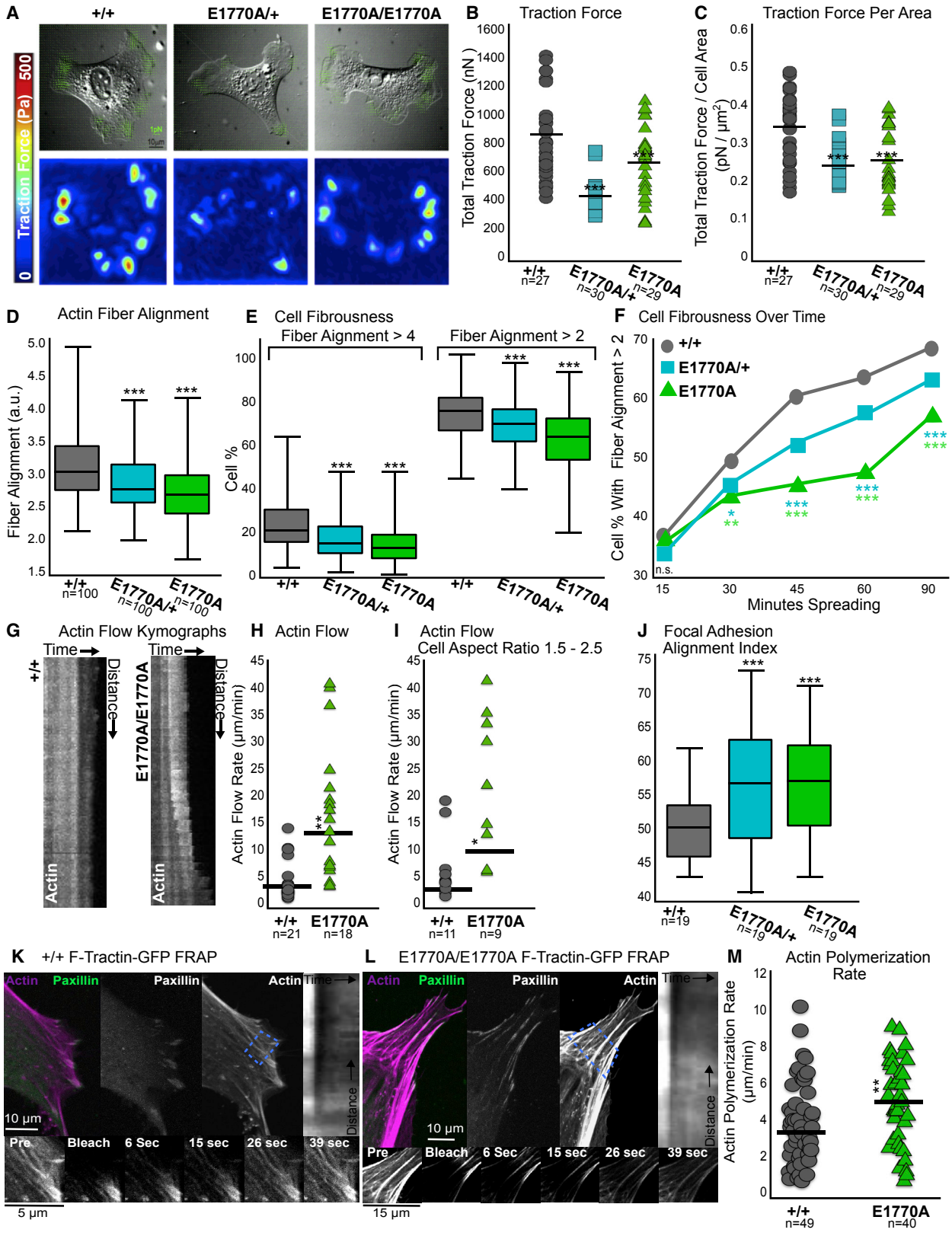

(legend on next page)

stability of FAs. Not all of these changes are congruous. For example, in *Tln1*^{E1770A} mutant MEFs, we observed not only that Talin was stabilized at adhesions compared to wild-type but also that there were fewer total adhesions, fewer nascent adhesions, and increased actin dynamics. These results suggest that in the wild-type, autoinhibition negatively regulates the stability of Talin at the membrane but promotes the formation of nascent adhesions and actin dynamics. How can we reconcile these disparate observations? One possibility is that the increased residence of E1770A in FAs relative to the wild-type is sequestering Talin in such a way that it is then unavailable to form nascent adhesions and support cell spreading. This scenario illustrates how even a potentially minor change in the regulation of Talin can alter the precisely regulated steady state that is required for proper adhesion and lead to diverse phenotypes in cell-ECM adhesion.

The relationships among cell-ECM adhesion, actin cytoskeleton dynamics, and traction force are well established (Parsons et al., 2010). Talin, which links ECM-bound integrins to the actin cytoskeleton, is needed to slow actin retrograde flow, produce traction forces, and stiffen cells in response to tension (Case and Waterman, 2015; Zhang et al., 2008). Integrin activation, which is increased *Tln1*^{E1770A} mutants, has been shown to increase cell traction forces (Lin et al., 2013). It is therefore surprising that we find increased actin dynamics and lower traction force in *Tln1*^{E1770A} mutants. There are several possible explanations. First, it has been proposed that cell geometry and spread area, rather than factors like substrate stiffness or adhesion density, are key determinants of traction force (Oakes et al., 2014). Specifically, increased cell aspect ratio correlates with increased traction force. We show that *Tln1*^{E1770A} mutant MEFs are more circular than *Tln1*$^{+/+}$ MEFs. This is consistent with lower traction force if geometry is the key regulator of traction stress. Second, the correlation between FA size and traction force is not a simple linear relationship. For example, strongly reducing myosin contractility does not significantly affect FA composition during maturation, knocking down α-actinin increases traction force but decreases FA size (Oakes et al., 2014), and depletion of vinculin decreases traction force but increases FA size. In particular, using vinculin mutants with defects in actin binding, it was demonstrated that FA growth is directly proportional to actin flow rate (Thievessen et al., 2013). These phenotypes bear a striking resemblance to those we describe in the *Tln1*^{E1770A} mutants. Third, the interaction between Kank2 and Talin has been shown to modulate Talin-actin binding and traction force generation (Sun et al., 2016; Bouchet et al., 2016). It is possible that the *Tln1*^{E1770A} mutation affects Kank2-Talin interactions, thus altering actin dynamics. We conclude that while at this point the precise mechanisms underlying the biomechanical phenotypes resulting from compromised talin autoinhibition are unknown, these likely involve changes in cell geometry and/or the ability of actin to associate with the adhesion complex. Overall, our data show that regulating integrin-mediated adhesion via talin autoinhibition can be used to modulate actin dynamics and the biomechanical properties of tissues.

STAR★METHODS

Detailed methods are provided in the online version of this paper and include the following:

- KEY RESOURCES TABLE
- CONTACT FOR REAGENT AND RESOURCE SHARING
- EXPERIMENTAL MODEL AND SUBJECT DETAILS
- METHOD DETAILS
  - Biochemistry
  - qRT-PCR
  - Primary Cell Culture
  - siRNA Knockdown & Western Blotting
  - Antibodies & Immunofluorescence
  - Live Cell Imaging
  - Relative Adhesive Strength
  - Scratch Assays
  - Biopsy Wound Assay

Figure 7. Talin Autoinhibition Regulates Actin Organization and Traction Force in MEFs

(A) Representative traction force microscopy (TFM) images. Top: overlaid with traction vectors. Bottom: traction heatmaps.

(B) Total traction force per cell, with the black line as the mean.

(C) Total traction force per square micrometer of cell area, with the black line as the mean.

(D) Actin fiber alignment of phalloidin-stained MEFs plated on fibronectin. n values represent numbers of cells and are the same for (E).

(E) Cell fibrousness, defined as the percentage of the cell with an actin fiber alignment above a strict (>4) or relaxed (>2) cutoff.

(F) Average cell fibrousness over time with a relaxed (>2) cutoff. n values are the same as in Figure 5B.

(G) Representative kymographs generated from F-tractin-GFP-labeled cells imaged for 15 min at 1 s/frame. Kymographs were generated from lines drawn through active protrusions.

(H) Actin flow rate determined from kymographs, with the black line as the mean. n values represent numbers of cells.

(I) Actin flow rate determined from kymographs from cells with aspect ratios ranging from 1.5 to 2.5. The black line represents the mean, and n values represent numbers of cells.

(J) FA alignment index per cell, defined as 90° minus the difference between individual FA angles from the reference FA angle, so high FAAI equates to high global alignment (Wu et al., 2012).

(K) Representative images of the leading edge of *Tln1*$^{+/+}$ MEFs plated on fibronectin and transfected with paxillin-mCherry (green and white) and F-tractin-GFP (magenta and white). ROIs encompassing dorsal stress fibers were bleached, and recovery was imaged over time. Kymographs of the recovery were made, and the angle of the contrast boundary was used to determine the actin flow rate.

(L) Representative images of the leading edge of *Tln1*$^{E1770A/E1770A}$ MEFs plated on fibronectin and transfected with paxillin-mCherry (green and white) and F-tractin-GFP (magenta and white). ROIs encompassing dorsal stress fibers were bleached, and recovery was imaged over time. Kymographs of the recovery were made, and the angle of the contrast boundary was used to determine the actin flow rate.

(M) Actin polymerization rate determined from kymographs, with the black line as the mean. n values represent numbers of cells.

All error bars denote SEM, with ***p $\leq$ 0.0001, **p $\leq$ 0.001, and *p $\leq$ 0.01.

SUPPLEMENTAL INFORMATION

Supplemental Information includes four figures and can be found with this article online at https://doi.org/10.1016/j.celrep.2018.10.098.

ACKNOWLEDGMENTS

This study was supported by CIHR Operating Grants to G.T. (MOP-285391) and L.L. (MOP-119357), a CIHR grant-in-aid to D.J.G., a CIHR post-doctoral fellowship to C.T.T., a Canada Foundation for Innovation Grant to S.P. (#34473), and NSERC Discovery Grants to L.L. (386979-12) and S.P (RGPIN-2015-05114). In addition, B.T.G is funded by Biotechnology and Biological Sciences Research Council grant (BB/N007336/1) and B.T.G and A.W are funded by a Human Frontier Science Program grant (RGP00001/2016).

AUTHOR CONTRIBUTIONS

A.H. and G.T. conceived this study. A.H. performed all cell and mouse experiments, with the exception of traction force microscopy performed by S.P. A.W. and B.T.G. performed all biochemistry experiments. D.C. performed qRT-PCR experiments. K.G. developed MATLAB scripts for automated image analysis of fixed FA morphology, cell morphology, and actin fibers. A.B. and L.L. provided reagents and expertise in training for primary cell culture and mouse husbandry. C.T.T. and D.J.G. provided expertise and guidance on *in vivo* wound healing assays. A.H. and G.T. wrote this manuscript, with contributions from all other co-authors.

DECLARATION OF INTERESTS

The authors declare no competing interests.

Received: April 18, 2018
Revised: September 7, 2018
Accepted: October 25, 2018
Published: November 27, 2018

REFERENCES

Ballestrem, C., Hinz, B., Imhof, B.A., and Wehrle-Haller, B. (2001). Marching at the front and dragging behind: differential alphaVbeta3-integrin turnover regulates focal adhesion behavior. J. Cell Biol. *155*, 1319–1332.

Banno, A., Goult, B.T., Lee, H., Bate, N., Critchley, D.R., and Ginsberg, M.H. (2012). Subcellular localization of talin is regulated by inter-domain interactions. J. Biol. Chem. *287*, 13799–13812.

Bazzoni, G., Shih, D.T., Buck, C.A., and Hemler, M.E. (1995). Monoclonal antibody 9EG7 defines a novel beta 1 integrin epitope induced by soluble ligand and manganese, but inhibited by calcium. J. Biol. Chem. *270*, 25570–25577.

Belin, B.J., Goins, L.M., and Mullins, R.D. (2014). Comparative analysis of tools for live cell imaging of actin network architecture. Bioarchitecture *4*, 189–202.

Berginski, M.E., Vitriol, E.A., Hahn, K.M., and Gomez, S.M. (2011). High-resolution quantification of focal adhesion spatiotemporal dynamics in living cells. PLoS ONE *6*, e22025.

Bouchet, B.P., Gough, R.E., Ammon, Y.C., van de Willige, D., Post, H., Jacquemet, G., Altelaar, A.M., Heck, A.J.R., Goult, B.T., and Akhmanova, A. (2016). Talin-KANK1 interaction controls the recruitment of cortical microtubule stabilizing complexes to focal adhesions. eLife *5*, e18124.

Brown, N.H., Gregory, S.L., Rickoll, W.L., Fessler, L.I., Prout, M., White, R.A., and Fristrom, J.W. (2002). Talin is essential for integrin function in *Drosophila*. Dev. Cell *3*, 569–579.

Calderwood, D.A. (2004a). Integrin activation. J. Cell Sci. *117*, 657–666.

Calderwood, D.A. (2004b). Talin controls integrin activation. Biochem. Soc. Trans. *32*, 434–437.

Calderwood, D.A., Zent, R., Grant, R., Rees, D.J., Hynes, R.O., and Ginsberg, M.H. (1999). The Talin head domain binds to integrin beta subunit cytoplasmic tails and regulates integrin activation. J. Biol. Chem. *274*, 28071–28074.

Case, L.B., and Waterman, C.M. (2015). Integration of actin dynamics and cell adhesion by a three-dimensional, mechanosensitive molecular clutch. Nat. Cell Biol. *17*, 955–963.

Cetera, M., Ramirez-San Juan, G.R., Oakes, P.W., Lewellyn, L., Fairchild, M.J., Tanentzapf, G., Gardel, M.L., and Horne-Badovinac, S. (2014). Epithelial rotation promotes the global alignment of contractile actin bundles during *Drosophila* egg chamber elongation. Nat. Commun. *5*, 5511.

Clark, E.A., and Brugge, J.S. (1995). Integrins and signal transduction pathways: the road taken. Science *268*, 233–239.

Critchley, D.R. (2009). Biochemical and structural properties of the integrin-associated cytoskeletal protein talin. Annu. Rev. Biophys. *38*, 235–254.

Debrand, E., Jai, Y.E., Spence, L., Bate, N., Praekelt, U., Pritchard, C.A., Monkley, S.A., and Critchley, D.R. (2009). Talin 2 is a large and complex gene encoding multiple transcripts and protein isoforms. FEBS J. *6*, 1610–1628.

Ellis, S.J., Goult, B.T., Fairchild, M.J., Harris, N.J., Long, J., Lobo, P., Czerniecki, S., Van Petegem, F., Schöck, F., Peifer, M., and Tanentzapf, G. (2013). Talin autoinhibition is required for morphogenesis. Curr. Biol. *23*, 1825–1833.

Ganguli-Indra, G. (2014). Protocol for cutaneous wound healing assay in a murine model. Methods Mol. Biol. *1210*, 151–159.

García, A.J., Ducheyne, P., and Boettiger, D. (1997). Quantification of cell adhesion using a spinning disc device and application to surface-reactive materials. Biomaterials *18*, 1091–1098.

Gardel, M.L., Sabass, B., Ji, L., Danuser, G., Schwarz, U.S., and Waterman, C.M. (2008). Traction stress in focal adhesions correlates biphasically with actin retrograde flow speed. J. Cell Biol. *183*, 999–1005.

Geiger, B., and Yamada, K.M. (2011). Molecular architecture and function of matrix adhesions. Cold Spring Harb. Perspect. Biol. *3*, a005033.

Ginsberg, M.H. (2014). Integrin activation. BMB Rep. *47*, 655–659.

Goksoy, E., Ma, Y.-Q.Q., Wang, X., Kong, X., Perera, D., Plow, E.F., and Qin, J. (2008). Structural basis for the autoinhibition of talin in regulating integrin activation. Mol. Cell *31*, 124–133.

Goodwin, K., Ellis, S.J., Lostchuck, E., Zulueta-Coarasa, T., Fernandez-Gonzalez, R., and Tanentzapf, G. (2016). Basal cell-extracellular matrix adhesion regulates force transmission during tissue morphogenesis. Dev. Cell *39*, 611–625.

Goult, B.T., Bate, N., Anthis, N.J., Wegener, K.L., Gingras, A.R., Patel, B., Barsukov, I.L., Campbell, I.D., Roberts, G.C., and Critchley, D.R. (2009). The structure of an interdomain complex that regulates talin activity. J. Biol. Chem. *284*, 15097–15106.

Goult, B.T., Xu, X.-P.P., Gingras, A.R., Swift, M., Patel, B., Bate, N., Kopp, P.M., Barsukov, I.L., Critchley, D.R., Volkmann, N., and Hanein, D. (2013). Structural studies on full-length talin1 reveal a compact auto-inhibited dimer: implications for talin activation. J. Struct. Biol. *184*, 21–32.

Horwitz, A., Duggan, K., Buck, C., Beckerle, M.C., and Burridge, K. (1986). Interaction of plasma membrane fibronectin receptor with talin—a transmembrane linkage. Nature *320*, 531–533.

Iwamoto, D.V., and Calderwood, D.A. (2015). Regulation of integrin-mediated adhesions. Curr. Opin. Cell Biol. *36*, 41–47.

Kanchanawong, P., Shtengel, G., Pasapera, A.M., Ramko, E.B., Davidson, M.W., Hess, H.F., and Waterman, C.M. (2010). Nanoscale architecture of integrin-based cell adhesions. Nature *468*, 580–584.

Kim, M., Carman, C.V., and Springer, T.A. (2003). Bidirectional transmembrane signaling by cytoplasmic domain separation in integrins. Science *301*, 1720–1725.

Klapholz, B., and Brown, N.H. (2017). Talin—the master of integrin adhesions. J. Cell Sci. *130*, 2435–2446.

Kopp, P.M., Bate, N., Hansen, T.M., Brindle, N.P., Praekelt, U., Debrand, E., Coleman, S., Mazzeo, D., Goult, B.T., Gingras, A.R., et al. (2010). Studies on the morphology and spreading of human endothelial cells define key inter- and intramolecular interactions for talin1. Eur. J. Cell Biol. *89*, 661–673.

Lee, H.-S.S., Anekal, P., Lim, C.J., Liu, C.-C.C., and Ginsberg, M.H. (2013). Two modes of integrin activation form a binary molecular switch in adhesion maturation. Mol. Biol. Cell *24*, 1354–1362.

Li, B., and Wang, J.H. (2011). Fibroblasts and myofibroblasts in wound healing: force generation and measurement. J. Tissue Viability *20*, 108–120.

Liang, C.-C.C., Park, A.Y., and Guan, J.-L.L. (2007). *In vitro* scratch assay: a convenient and inexpensive method for analysis of cell migration *in vitro*. Nat. Protoc. *2*, 329–333.

Lin, G.L., Cohen, D.M., Desai, R.A., Breckenridge, M.T., Gao, L., Humphries, M.J., and Chen, C.S. (2013). Activation of beta 1 but not beta 3 integrin increases cell traction forces. FEBS Lett. *587*, 763–769.

Martin, P., and Parkhurst, S.M. (2004). Parallels between tissue repair and embryo morphogenesis. Development *131*, 3021–3034.

Maruthamuthu, V., Sabass, B., Schwarz, U.S., and Gardel, M.L. (2011). Cell-ECM traction force modulates endogenous tension and cell-cell contacts. Proc. Natl. Acad. Sci. USA *108*, 4708–4713.

Monkley, S.J., Zhou, X.H., Kinston, S.J., Giblett, S.M., Hemmings, L., Priddle, H., Brown, J.E., Pritchard, C.A., Critchley, D.R., and Fässler, R. (2000). Disruption of the talin gene arrests mouse development at the gastrulation stage. Dev. Dyn. *219*, 560–574.

Munevar, S., Wang, Y.L., and Dembo, M. (2001). Distinct roles of frontal and rear cell-substrate adhesions in fibroblast migration. Mol. Biol. Cell *12*, 3947–3954.

Narasimha, M., and Brown, N.H. (2004). Novel functions for integrins in epithelial morphogenesis. Curr. Biol. *14*, 381–385.

Oakes, P.W., Banerjee, S., Marchetti, M.C., and Gardel, M.L. (2014). Geometry regulates traction stresses in adherent cells. Biophys. J. *107*, 825–833.

Oh-McGinnis, R., Bogutz, A.B., Kang, Y.L., Higgins, M.J., and Lefebvre, L. (2010). Rescue of placental phenotype in a mechanistic model of Beckwith-Wiedemann syndrome. BMC. Dev. Biol. *10*, 50.

Parsons, J.T., Horwitz, A.R., and Schwartz, M.A. (2010). Cell adhesion: integrating cytoskeletal dynamics and cellular tension. Nat. Rev. Mol. Cell Biol. *11*, 633–643.

Priddle, H., Hemmings, L., Monkley, S., Woods, A., Patel, B., Sutton, D., Dunn, G.A., Zicha, D., and Critchley, D.R. (1998). Disruption of the talin gene compromises focal adhesion assembly in undifferentiated but not differentiated embryonic stem cells. J. Cell Biol. *142*, 1121–1133.

Romsey, N.R., Hou, Y., Lara Rodriguez, L., and Schneider, I.C. (2014). The number of lines a cell contacts and cell contractility drive the efficiency of contact guidance. Cell. Mol. Bioeng. *7*, 122–135.

Sabass, B., Gardel, M.L., Waterman, C.M., and Schwarz, U.S. (2008). High resolution traction force microscopy based on experimental and computational advances. Biophys. J. *94*, 207–220.

Sakar, M.S., Eyckmans, J., Pieters, R., Eberli, D., Nelson, B.J., and Chen, C.S. (2016). Cellular forces and matrix assembly coordinate fibrous tissue repair. Nat. Comm. *7*, 11036.

Schindelin, J., Arganda-Carreras, I., Frise, E., Kaynig, V., Longair, M., Pietzsch, T., Preibisch, S., Rueden, C., Saalfeld, S., Schmid, B., et al. (2012). Fiji: an open-source platform for biological-image analysis. Nat. Methods. *7*, 676–682.

Shattil, S.J., O'Toole, T., Eigenthaler, M., Thon, V., Williams, M., Babior, B.M., and Ginsberg, M.H. (1995). β_3-endonexin, a novel polypeptide that interacts specifically with the cytoplasmic tail of the integrin β_3 subunit. J. Cell Biol. *131*, 807–816.

Song, X., Yang, J., Hirbawi, J., Ye, S., Perera, H.D., Goksoy, E., Dwivedi, P., Plow, E.F., Zhang, R., and Qin, J. (2012). A novel membrane-dependent on/off switch mechanism of talin FERM domain at sites of cell adhesion. Cell Res. *22*, 1533–1545.

Sun, Z., Tseng, H.Y., Tan, S., Senger, F., Kurzawa, L., Dedden, D., Mizuno, N., Wasik, A.A., Thery, M., Dunn, A.R., and Fässler, R. (2016). Kank2 activates talin, reduces force transduction across integrins and induces central adhesion formation. Nat. Cell Biol. *18*, 941–953.

Tadokoro, S., Shattil, S.J., Eto, K., Tai, V., Liddington, R.C., de Pereda, J.M., Ginsberg, M.H., and Calderwood, D.A. (2003). Talin binding to integrin beta tails: a final common step in integrin activation. Science *302*, 103–106.

Thievessen, I., Thompson, P.M., Berlemont, S., Plevock, K.M., Plotnikov, S.V., Zemljic-Harpf, A., Ross, R.S., Davidson, M.W., Danuser, G., Campbell, S.L., and Waterman, C.M. (2013). Vinculin-actin interaction couples actin retrograde flow to focal adhesions, but is dispensable for focal adhesion growth. J. Cell Biol. *202*, 163–177.

Tojkander, S., Gateva, G., Husain, A., Krishnan, R., and Lappalainen, P. (2015). Generation of contractile actomyosin bundles depends on mechanosensitive actin filament assembly and disassembly. eLife *10*, e06126.

Tomasek, J.J., Gabbiani, G., Hinz, B., Chaponnier, C., and Brown, R.A. (2002). Myofibroblasts and mechano-regulation of connective tissue remodelling. Nat. Rev. Mol. Cell Biol. *3*, 349–363.

Tschammer, N., Galinec, S., Weigert, S., Muller, Y., You, C., Piehler, J., and Breitsprecher, D. (2016). Protein labeling one-step, purification-free and site-specific labeling of polyhistidine-tagged proteins for MST. Protein Labeling Application Note NT-MO-29. https://www.researchgate.net/publication/311582381_Protein_Labeling_One-step_purification-free_and_site-specific_labeling_of_polyhistidine-tagged_proteins_for_MST.

Wingate, A.D., Martin, K.J., Hunter, C., Carr, J.M., Clacher, C., and Arthur, J.S. (2009). Generation of a conditional CREB Ser133Ala knockin mouse. Genesis *47*, 688–696.

Wolfenson, H., Henis, Y.I., Geiger, B., and Bershadsky, A.D. (2009). The heel and toe of the cell's foot: a multifaceted approach for understanding the structure and dynamics of focal adhesions. Cell Motil. Cytoskeleton *66*, 1017–1029.

Wolfenson, H., Lavelin, I., and Geiger, B. (2013). Dynamic regulation of the structure and functions of integrin adhesions. Dev. Cell *24*, 447–458.

Wu, C., Asokan, S.B., Berginski, M.E., Haynes, E.M., Sharpless, N.E., Griffith, J.D., Gomez, S.M., and Bear, J.E. (2012). Arp2/3 is critical for lamellipodia and response to extracellular matrix cues but is dispensable for chemotaxis. Cell *148*, 973–987.

Zhang, X., Jiang, G., Cai, Y., Monkley, S.J., Critchley, D.R., and Sheetz, M.P. (2008). Talin depletion reveals independence of initial cell spreading from integrin activation and traction. Nat. Cell Biol. *10*, 1062–1068.

Zhang, H., Chang, Y.-C.C., Huang, Q., Brennan, M.L., and Wu, J. (2016). Structural and functional analysis of a talin triple-domain module suggests an alternative talin autoinhibitory configuration. Structure *24*, 721–729.

STAR★METHODS

KEY RESOURCES TABLE

REAGENT or RESOURCE	SOURCE	IDENTIFIER
Antibodies		
Talin-1	Santa Cruz	YQ-16; RRID:AB_2303406
Paxillin	BD	349/Paxillin; RRID:AB_397464
β1-integrin total	R&D	Gln21-Ala738; RRID:AB_416591
β1-integrin active	BD	9EG7; RRID:AB_393729
FAK	BD	77/FAK; RRID:AB_397494
pTyr397FAK	Thermo-Fisher	31H5L17; RRID:AB_2533701
Talin-2	Abcam	68E7
β-tubulin	DHSB	E7; RRID:AB_528499
Chemicals, Peptides, and Recombinant Proteins		
β1a-integrin (752-798)	Ben Goult	N/A
Tln1 WT	Ben Goult	N/A
Tln1 E1770A	Ben Goult	N/A
Critical Commercial Assays		
Tln2 ON-TARGET plus SMARTpool	Dharmacon	L-065877-00-0005
ON-TARGET plus Non-targeting Pool	Dharmacon	D-001810-10-05
Deposited Data		
F3:R9 talin interaction complex	Song et al., 2012	PDB: 4F7G
Experimental Models: Organisms/Strains		
Tln1^{E1770A} Mice	Genoway	*Tln1*^{E1770A}
Oligonucleotides		
Primer: *Tln1*^{E1770A} Mice Genotyping Forward: 5′ACTAAGACATCGA AGGCTGGGATATGCTG3′	Genoway / This paper	N/A
Primer: *Tln1*^{E1770A} Mice Genotyping Reverse: 5′GTCAGGTACTGTT AACCTATCTCCTCAGCTCC3′.	Genoway / This paper	N/A
Primer: Tln1 qRT Forward: 5′AGCTTTCCAAGAAGTGG3′	This Paper	N/A
Primer: Tln1 qRT Reverse: 5′TTCTGAAGGGTCAGCAGCAC3′.	This Paper	N/A
Primer: Tln2 qRT Forward: 5′GGATAGGGCCACCATTTTCA3′	Debrand et al., 2009	a
Primer: Tln2 qRT Reverse: 5′GCTCCGCAATGAGACAGTAGCT3′.	Debrand et al., 2009	b
Primer: Ppia qRT Forward: 5′CGCGTCTCCTTCGAGCTGTTTG3′	Oh-McGinnis et al., 2010	N/A
Primer: Ppia qRT Forward: 5′TGTAAAGTCACCACCCTGGCACAT3′	Oh-McGinnis et al., 2010	N/A
Recombinant DNA		
Tln1-GFP	Chinten James Lim	N/A
E1770A Tln1-GFP	Ben Goult	N/A
F-tractin-GFP	Sergey Plotnikov	N/A
mCherry-paxillin	Mike Gold	N/A
paxillin-GFP	Addgene	#15233
Software and Algorithms		
MATLAB	Commercial	https://www.mathworks.com/products/matlab.html
Focal Adhesion Analysis Server	Berginski et al., 2011	http://faas.bme.unc.edu/
FIJI	Schindelin et al., 2012	https://fiji.sc/

CONTACT FOR REAGENT AND RESOURCE SHARING

Further information and requests for resources and reagents should be directed to and will be fulfilled by the Lead Contact, Guy Tanentzapf (tanentz@mail.ubc.ca).

EXPERIMENTAL MODEL AND SUBJECT DETAILS

Tln1^{E1770A} mice were generated by Genoway S.A. (France) on the C57BL/6J genetic background. A Cre-activated mini gene approach was used (Wingate et al., 2009). Briefly, a targeting construct was used containing a hybrid of genomic DNA and cDNA containing the entire wild-type *Tln1* sequence from exons 41 to the terminal coding exon 59, followed by a polyadenylation cDNA sequence. Prior to Cre-mediated recombination, wild-type *Tln1* is transcribed through the endogenous promoter using this mini gene. After Cre-mediated recombination, the mini gene is excised and mutant *Tln1*^{E1770A} is transcribed using the endogenous promoter. To create the conventional point mutated (*Tln1*^{E1770A}) allele we used a ubiquitous Cre-deleter (pCMV-Cre) line that expresses Cre in the germ cells to make a permanently recombined line. This conventional, point-mutated allele, *Tln1*^{E1770A}, was used for all subsequent experiments. Mice were genotyped at weaning using the following primers at 65°C annealing temperature: 5′ACTAAGACATCGAAGGCTGGGATATGCTG3′ and 5′GTCAGGTACTGTTAACCTATCTCCTCAGCTCC3′. These produced a 451bp mutant band and a 381bp wild-type band. All animals were housed at the Centre for Disease Modeling at the University of British Columbia using standard husbandry. The University of British Columbia Animal Care and Use Program approved all procedures. *Tln1*$^{E1770A/+}$ intercrosses were set up at 7 weeks of age, only the first three litters of each breeding pair was included in progeny counts. Images of male mice were taken between 18 and 22 weeks of age post-euthanasia for presentation and body length measurements. Littermate males were weighed weekly on the same day at approximately the same time.

METHOD DETAILS

Biochemistry

Purification of Recombinant Polypeptides

Full length mouse Tln1, wild-type and E1770A mutants, were cloned into a pET21a vector, and the cytoplasmic tail of β1a-integrin (752-798) was cloned into a pET151 vector (Invitrogen) and expressed in E.coli BL21(DE3) cells cultured in LB. Standard nickel-affinity chromatography was used to purify the His-tagged recombinant proteins as described previously (Banno et al., 2012). β1a-Integrin was further purified using anion-exchange chromatography following cleavage of the 6xHIS-tag with TEV protease. The talin constructs were further purified and analyzed using a HiLoad 16/600 Superdex 200 size exclusion chromatography column (GE healthcare). 5 mL of sample was loaded and run at 0.5 ml/min flow rate at 4°C in 50 mM Tris, 150 mM NaCl, 2mM DTT. Purified samples were further analyzed by SDS-PAGE on a 10% gel and stained using Coomasie blue. Protein concentrations were determined using the respective extinction coefficients at 280nm calculated using ProtParam.

Microscale Thermophoresis

Tln1 was coupled to an equimolar amount of NT-647 dye (RED-tris-NTA, NanoTemper) via its C-terminal 6xHis-Tag in a one-step coupling reaction (Tschammer et al., 2016). Titrations were performed in phosphate buffered saline (PBS; 137 mM NaCl, 27 mM KCl, 100 mM Na_2HPO_4, 18 mM KH_2PO_4) using a constant 50 nM concentration of RED-tris-NTA coupled Tln1, with an increasing concentration of recombinant β1a-integrin peptide; final volume 20 μl. Prepared samples were loaded into Monolith NT.115 Capillaries (NanoTemper) and measurements were recorded on a Monolith NT.115 at 25°C, excited under red light with medium MST power and 40% excitation power. The data was analyzed using MO Affinity Analysis software and fitted using the K_d fit model.

qRT-PCR

Total RNA was isolated from MEFs in culture using TRIzol. A total of 0.5 μg total RNA was converted into cDNA using a qScript cDNA Synthesis Kit (Quanta Biosciences). Subsequently, qPCR was performed using iQ SYBR Green Supermix (BIORAD). Tln1 & Tln2 mRNA levels was averaged between three independent experiments performed four times and normalized to Ppia (Peptidyl Prolyl Isomerase A) expression. Primers used for Ppia are as follows: 5′CGCGTCTCCTTCGAGCTGTTTG3′ and 5′TGTAAAGTCACC ACCCTGGCACAT3′ Primers used for Tln1 are as follows: 5′AGCTTTCCAAGAAGTGG3′ and 5′TTCTGAAGGGTCAGCAGCAC3′. Primers used for Tln2 are as follows: 5′GGATAGGGCCACCATTTTCA3′ and 5′GCTCCGCAATGAGACAGTAGCT3′.

Primary Cell Culture

Primary MEFs were isolated from E13.5 embryos. MEFs were plated on 0.1% gelatin in Dulbecco's Modified Eagle's Medium (DMEM) supplemented with 10% Fetal Bovine Serum, 1% penicillin-streptomycin (15140122 Thermo-Fisher), 2mM L-Glutamine, and 1mM Sodium Pyruvate. Cells were used for experiments up to passage 5.

siRNA Knockdown & Western Blotting

For siRNA mediated knockdown of Tln2, a ON-TARGET plus SMARTpool (L-065877-00-0005) was used. A ON-TARGET plus Non-targeting Pool (D-001810-10-05) was used for controls. MEFs were plated on either 0.1mg/ml fibronectin coated coverslips

or in gelatin coated 6-well plates for 90 minutes before transfection with siRNA. Cells were then incubated overnight before being stained (see below for immunofluorescence) or collected for western blotting. Protein samples were isolated via TRIzol combining 3 wells of a 6-well plate per sample and were resolved using a 7% gel. Primary antibody used: 1:500 Tln2 (68E7, Abcam) and 1:500 β-tubulin (E7, DHSB). Secondary antibody used: 1:3000 anti-mouse-HRP (Biorad). Chemiluminescent substrate (Clarity Western ECL Biorad) was applied via manufacturer instruction and blots were exposed to X-ray film.

Antibodies & Immunofluorescence

For immunofluorescence stains, MEFs were plated on 0.1mg/ml fibronectin-coated coverslips for 90 minutes (unless otherwise indicated). Cells were fixed with 4% paraformaldehyde for 15 minutes at room temperature. Cells were then permeabilized with 0.3% Triton-X for 5 minutes at room temperature, blocked with 1% BSA with 1:200 Rhodamine-Phallodin or Alexafluor 633-Phallodin for 60 minutes at room temperature, incubated with primary antibody (with or without 1% BSA) for 180 minutes at room temperature, and finally incubated with secondary antibody diluted in PBS for 60 minutes at room temperature. Between each step slides were washed 3 times for 5 minutes at room temperature with PBS. Slides were then mounted with vectashield containing a DAPI stain. Primary antibody dilutions used: 1:100 Talin-1 (with BSA, YQ-16 Santa Cruz), Paxillin (349/Paxillin BD), β1-integrin total (Gln21-Ala738, R&D), β1-integrin active (9EG7 BD), 1:200 FAK (77/FAK BD), 1:200 pTyr397FAK (31H5L17 Thermo-Fisher). Z stack images were taken with an Olympus Fluoview (FV1000) inverted confocal microscope at 0.5 μm slice thickness and 2048 resolution.

Live Cell Imaging

Fluorescence Recovery After Photobleaching (FRAP)

MEFs were plated on 0.1mg/ml fibronectin coated coverslips. After spreading for 90 minutes cells were transfected with paxillin-GFP (Addgene #15233), Tln1-GFP (from Chinten James Lim), E1770A Tln1-GFP (from B.T.G), mCherry-paxillin (from Mike Gold), and/or F-tractin-GFP (from S.P.). Cells were incubated overnight before imaging at 37°C on an Olympus Fluoview (FV1000) inverted confocal microscope. Small portions of the cell edge were bleached using the Tornado scanning tool (Olympus) with a 405nm laser at 100% power.

Total Internal Reflection Fluorescence (TIRF)

MEFs were plated on 0.1mg/ml fibronectin coated coverslips. After spreading for 90 minutes cells were transfected with paxillin-GFP (Addgene #15233). For post-spread analysis, cells were incubated overnight before being imaged using an Olympus IX83 automated inverted microscopy with an Olympus CellTIRF system. For during spreading analysis, cells were incubated overnight, then trypsinized and plated onto a 0.1mg/ml fibronectin coated coverslip for 15 minutes before imaging. Cells were imaged at 37°C every 1 minute for 60 minutes at 100X using a penetration depth of 60nm.

Traction Force Microscopy (TFM)

Traction force microscopy was performed as described previously (Sabass et al., 2008). Briefly, elastic polyacrylamide substrates (8.6kPa shear modulus, ≈20 μm gel thickness) with embedded 40nm red and far-red fluorescent beads (Invitrogen) were prepared on glass coverslips and the top surface of the substrates was functionalized with 1mg/mL human plasma fibronectin (Millipore) to facilitate cell attachment. Cells were plated on fibronectin-coupled polyacrylamide substrates. After spreading for 120 minutes, the coverslips were mounted in a perfusion chamber (RC30, Warner Instruments), and a series of DIC images of the cells and fluorescent images of the beads within the substrate were acquired by a spinning disk confocal microscope (Nikon Ti2 equipped with CSUX10 confocal head and Photometrics Myo CCD camera). The cells were removed from the substrate by perfusing 5 mL of 0.5% phenol red-free trypsin-EDTA (Thermo) into the chamber, and an image of beads in the unstrained substrate was captured.

Relative Adhesive Strength

We used a method adapted from García et al. (1997) that has been previously published by Romsey et al. (2014). MEFs were plated on 0.1mg/ml fibronectin-coated coverslips for 90 minutes. Non-spun control coverslips were then fixed with 4% paraformaldehyde for 15 minutes at room temperature. Experimental coverslips were spun at 4000RPM while 1 mL of DMEM media was applied for approximately 15 s and then fixed. After fixing cells were permeabilized as described above and incubated with 1:200 AlexaFluor 488 Phallodin overnight. 20 fields of view of 5 different coverslips were imaged for each spun and non-spun condition at 20X using an Olympus Fluoview (FV1000) inverted confocal microscope.

Scratch Assays

MEFs were cultured in 6-well plates on 0.1% gelatin. When the cells formed a confluent monolayer a wound was introduced with a pipette tip (VWR 53508-810). Scratches were imaged over time under phase contrast with a Leica DMIL inverted microscope equipped with a QImaging MicroPublisher 5.0 RTV camera.

Biopsy Wound Assay

Littermate female mice were subjected to wounding at 8 weeks of age. Mice were anesthetized with isoflurane and then shaved and cleaned on the dorsal side. A single full thickness wound was then created on the dorsal side with a sterile 6mm biopsy punch. Prior to wounding mice received sub-cutaneous fluids, a Meloxicam sub-cutaneous injection at 5mg/kg, and a sub-cutaneous injection of Bupivacaine at 8mg/kg near the wound site. After wounding mice received sub-cutaneous injections of Meloxicam for at least

two days or longer depending on monitoring. Wounded mice were monitored daily for 14 days and imaged throughout with a digital Sony Cyber-shot camera.

QUANTIFICATION AND STATISTICAL ANALYSIS

Live Cell Imaging

Fluorescence Recovery After Photobleaching (FRAP)

Movies for FRAP of FAs were then analyzed with ImageJ using a previously developed Jython script available at https://imagej.net/Analyze_FRAP_movies_with_a_Jython_script. Here, ROIs for analysis are chosen specifically drawn over FAs labeled in the pre-bleach time frames. Movies for FRAP of F-tractin-GFP were then analyzed with ImageJ using the Kymographbuilder plugin on lines drawn over dorsal stress fibers specifically.

Total Internal Reflection Fluorescence (TIRF)

Live FAs (Figures 4 and 7) were analyzed from TIRF movies (see above). Movies were submitted to the Focal Adhesion Analysis Server (Berginski et al., 2011) for analysis with standard settings used. Briefly, FAs are tracked throughout the movie and longevity refers to the number of minutes the FA persists. Static FA properties are also measured at each frame, including area. We defined nascent FAs as having longevity < 5 minutes and an area < 0.3 μm^2. We defined mature FAs as having a longevity > 15 minutes and an area > 1 μm^2. FA assembly and disassembly rates were determined by paxillin-GFP intensity values fit overtime to a log-linear model. The results only include FAs with positive rates and with model p values $\leq$ 0.05. These are presented as the slopes in Figure 4H. The length in minutes that each individual FA spent undergoing assembly or disassembly are presented as the length of the lines in Figure 4H. Stability phase length was determined as the amount of time between assembly and disassembly for each FA. The Focal Adhesion Alignment Index (FAAI) measure presented in Figure 7H was previously described by Wu et al., 2012. This is also determined from TIRF movies as analyzed by the Focal Adhesion Analysis Server. Briefly, the FAAI is a measure of the global alignment of FAs across the whole cell. FA angles are determined at each time point throughout imaging and the reference angle is determined as the angle that minimizes the deviation of FA angles across the whole cell. FAAI = 90 – standard deviation of adhesion angles at a particular reference angle. High FAAI = low standard deviation = high global alignment. Low FAAI = high standard deviation = low global alignment.

Traction Force Microscopy (TFM)

Correlation-based particle tracking velocimetry code in MATLAB was used to quantify the cell-induced deformation of the polyacrylamide gel. Deformations were interpolated onto a 0.47 μm displacement grid, and the stress field was reconstructed by Fourier-transformed traction cytometry and interpolated on a 0.47 μm grid (Sabass et al., 2008). To analyze total force exerted by a cell on the ECM, a binary cell mask was created by outlining cell boundaries manually and dilated by 50 pixels to include traction vectors that enter the region of interest (ROI), but whose origins lay just outside the ROI. Traction vectors outside the cell were defined as background forces and only vectors whose magnitudes greater than or equal to 2x above background were included in the analysis. The sum of traction stresses per square micrometer was calculated and multiplied by the area of the entire cell (Maruthamuthu et al., 2011).

Fixed Cell Imaging

Focal Adhesions (FAs)

Fixed FAs (Figures 2 and 3) were segmented using MATLAB. Briefly, confocal z-projections of single cells stained for FA markers were subject to difference of gaussians filtering in which background is reduced and smaller objects are enhanced. Filtered images were thresholded to generate a binary image in which individual bright objects containing more than 6 pixels were identified as FAs. From these images, we quantified FA number, area, and aspect ratio. To quantify intensity, the mask was applied to the original image and average pixel intensity was measured within each FA detected. For co-localization analysis, the mask obtained using one marker was then applied to the original image for another marker. We then extracted the list of individual pixel intensities within each FA for both markers, and computed the correlation coefficient between the two sets.

Cell Morphology

Cell contours were obtained automatically by processing confocal z-projections of cells stained for F-actin (Phallodin) in MATLAB. Images were first blurred with a Gaussian filter, then an edge detection algorithm was applied to identify cell borders. The resultant binary image was refined through successive dilations and erosions to yield the final cell contour. These contours were used to measure cell area, aspect ratio (long axis/short axis), and circularity (4πarea/perimeter^2). Morphology of cell protrusions was quantified automatically in MATLAB. First, cell contours were identified as outlined above. Next, we obtained the contour coordinates of the convex hull of the binary image representing cell area. At each point along the cell contour, we computed the minimum distance between the convex hull and the actual cell contour. Based on these distances, minima corresponding to protrusions could be identified. To be counted as protrusions, minima had to be at least 10 pixels apart along the contour and of height greater than 5 pixels. Based on the coordinates of adjacent peaks, the width, height, and aspect ratio of protrusions could be computed.

Actin Fibers

To quantitatively described actin fibers within cells, we adapted previously used methods (Cetera et al., 2014). First, we identified cell contours as described above. Next, the cell was subdivided into 32x32 pixel windows overlapping by 50%. We then computed the

two-dimensional Fourier transform of each window. If a window contains no fibers, the fourier transform will be a central, diffuse point of bright pixels. However, if a window contains aligned fibers, the fourier transform will consist of an elongated accumulation of bright pixels at a 90 degree angle to the original fibers. Based on the aspect ratio and orientation of the fourier transform, we determined fibrousness and fiber orientation in a given window. The data for individual windows could then be compared across the entire cell to estimate the cell fibrousness, defined here as the percentage of cell area (% of windows) with aspect ratio greater than a cut-off value.

Relative Adhesive Strength

Corresponding fields of view between non-spun control and spun experiments were compared. Cells were counted and relative adhesive strength is expressed as the percent of cells left in the spun experiment compared to the total number of cells in the relative same field of view in the non-spun control.

Scratch Assays & Wound Healing

ImageJ was then used to measure open wound area at each time point.

DATA AND SOFTWARE AVAILABILITY

The accession number for the structure of the F3:R9 talin interaction complex reported in this paper is PDB: 4F7G (Song et al., 2012). Other data are available from the Lead Contact upon reasonable request.